Minimum-Fuel Control Strategy for Spacecraft Formation Reconfiguration via Finite-Time Maneuvers

G. Di Mauro*
University of Florida, Gainesville, Florida 32611

D. Spiller†
Sapienza University of Rome, 00138 Rome, Italy

and

S. F. Rafano Carnà‡ and R. Bevilacqua§
University of Florida, Gainesville, Florida 32611

This paper addresses the minimum-fuel spacecraft formation reconfiguration maneuver in J_2 perturbed near-circular orbits. In this study, only the deputy is assumed to be maneuverable and capable of providing a piecewise constant control thrust. The optimal control problem is formulated as a mixed-integer linear programming problem. To make the proposed strategy compliant with the requirements deriving from a realistic flight scenario, the collision avoidance and the maneuvering time constraints dictated by mission operations are included in the mathematical formulation. A linear dynamics model based on relative orbit elements parameterization and its associated closed-form solution are used to impose the boundary conditions, avoiding the dynamics integration within the optimization process. Several examples are shown to demonstrate the effectiveness of the proposed approach.

I. Introduction

IN RECENT years, there has been an increasing interest in spacecraft formation flying concepts. In fact, the use of multiple spacecraft operating in a coordinated way allows improving the mission performance, while providing increased adaptability, versatility, and robustness. In light of this, different national space agencies, government research, and development centers as well as numerous universities and private companies have designed and funded more than 20 formation flying missions in the last two decades and plan to launch another 10 within the next 10 years [1].

Among the various technical challenges involved in spacecraft formation flying, the capability to reconfigure the relative motion represents a key aspect that has been intensively studied over the last years. The formation reconfiguration problem is defined as the achievement of a specific relative formation geometry in a defined time interval, given a general initial relative configuration. Thus far, many methods have been proposed to solve the aforementioned problem, ranging from the impulsive to the continuous control techniques. The impulsive approach for the satellite formation control has been widely discussed in many works. Gaias and D'Amico [2] addressed the problem of multi-impulsive solution schemes for formation reconfiguration in near-circular Keplerian orbits using relative orbit elements (ROEs). They proposed a general methodology, based on the inversion of relative dynamics equations, which led to the straightforward computation of

analytical or numerical control solutions. A similar impulsive approach based on the ROE parameterization is developed by Chernick and D'Amico in [3]. Here, the authors extended the results reported in [2], deriving the analytical and semi-analytical solutions for in-plane and out-of-plane reconfigurations, respectively, in near-circular J_2 perturbed and eccentric unperturbed orbits. Vaddi et al. [4] obtained a two-impulse analytical solution for the formation establishment and reconfiguration problems, using Gauss's variational equations (GVE) in terms of nonsingular elements. They demonstrated that the derived analytical solution is also fuel-optimal when only magnitudes of the relative eccentricity and inclination vectors are varied and the initial relative semimajor axis is null, comparing it with the result obtained using NPOPT, a numerical nonlinear optimization tool. Roscoe et al. [5] proposed an iterative method based on Lawden's primer vector theory to determine the n-impulse fuel-optimal maneuvers for the establishment and reconfiguration of spacecraft formations. The proposed method is valid in circular and elliptic orbits and includes first-order secular J_2 effects, whereas the dynamics is expressed in terms of differential mean orbital elements. The continuous methodology is implemented when the maneuverable satellites in the formation are equipped with low-thrust actuation system. Ben Larbi and Bergner [6] derived the nonimpulsive thrust maneuvers for formation reconfiguration in unperturbed circular orbits, using the relative orbit elements to describe the relative motion. Di Mauro et al. [7] derived a fully analytical solution for the in-plane reconfiguration with three tangential finite-time maneuvers by inverting the ROE-based linearized equations of relative motion. In addition, they proposed a semi-analytical approach to solve the out-of-plane satellite formation control problem with a single finite-time maneuver. Acikmese et al. [8] presented a convex guidance algorithm for optimal formation reconfiguration with collision avoidance using the Clohessy–Wiltshire–Hill equations. The collision avoidance constraints are imposed via separating planes between each pair of spacecraft. Moreover, a heuristic is introduced to choose these separating planes that leads to the convexification of the collision avoidance constraints. Huntington and Rao [9] proposed a fuel-optimal reconfiguration strategy for a tetrahedral formation. The reconfiguration problem was posed as a multiple-phase nonlinear optimal control problem and is solved via direct transcription using the Gauss pseudospectral method. Wu et al. [10] presented a method to determine the fuel-optimal low-thrust trajectories for satellite formation maneuvers in presence of J_2 effect. The resulting nonlinear optimal control problem is converted

*Postdoctoral Associate, Department of Mechanical and Aerospace Engineering, ADAMUS Laboratory, 939 Sweetwater Drive.

†Postdoctoral Fellow, School of Aerospace Engineering, via Salaria 851.

‡Graduate Research Assistant, Department of Mechanical and Aerospace Engineering, ADAMUS Laboratory, 939 Sweetwater Drive.

§Associate Professor, Department of Mechanical and Aerospace Engineering, ADAMUS Laboratory, 939 Sweetwater Drive. Senior Member AIAA.

into nonlinear programming (NLP) problem by the Legendre pseudospectral method. The NLP problem is then solved using a sparse nonlinear optimization algorithm. Richards et al. [11] proposed a fuel-optimal control strategy by using the linear time-varying Clohessy–Wiltshire–Hill relative dynamics model. The trajectory optimization approach was based on the solution of a mixed-integer linear programming (MILP) problem, including collision avoidance and thruster plume impingement constraints.

This paper addresses the design of the minimum-fuel spacecraft formation reconfiguration strategy in near-circular J_2-perturbed orbits. The associated optimal control problem is formulated as a MILP problem. Based on the linear programming, both constraints and the objective function must be linear. In light of this, the relative motion is described through a linear dynamics model based on ROE parameterization. To design a control strategy to be implemented in a realistic flight scenario, a collision avoidance constraint is included along with some operational constraints such as the minimum firing duration of the thrusters and the maximum number of performed finite-time maneuvers. The main advantage to translate the minimum-fuel problem into the MILP form is that a linear programming problem, even in the presence of a large number of variables and constraints, can be solved in a quite reasonable amount of time. The first contribution of this work is the development of an efficient algorithm for the design of the minimum-fuel reconfiguration maneuver for a two-satellite formation in near-circular J_2-perturbed orbits. The proposed method provides the finite-time maneuver strategy to control the relative trajectory, which has been proven to increase the final accuracy with respect to the impulsive counterpart [7]. Moreover, it is able to deal with a full formation reconfiguration problem (i.e., to handle the dynamics coupling between the in-plane and out-of-plane motion due to the J_2 perturbation). A further contribution is the inclusion of some additional constraints in the MILP formulation, such as the maximum number of finite-time maneuvers or the time constraints imposed by mission operations, to obtain a more flexible control scheme.

The reminder of this paper is organized as follows. In Sec. II, the ROE-based relative dynamics describing the satellite formation motion as well as its associated analytical solution is presented. In the same section, the optimization problem related to the design of the fuel-optimal reconfiguration maneuvering strategy is introduced. Section III shows the MILP formulation and details the equations for the considered constraints. The main results are reported in Sec. IV, pointing out the performance of proposed approach in terms of maneuver cost and accuracy and showing the computational burden of MILP solver.

II. Problem Statement

This section aims at defining the optimal control problem associated to the design of the minimum-fuel strategy for the formation flying reconfiguration. The full reconfiguration problem addressed in this study denotes the achievement of a specific in-plane and out-of-plane relative configuration in a given time interval. It must be observed that a full reconfiguration maneuver is required typically in specific operational scenarios as predocking v-bar approach or not passively safe close proximity operations.

First, the linear dynamics model describing the relative motion between two Earth-orbiting satellites is presented, along with the corresponding analytical solution. The proposed dynamics model is formulated using the dimensionless ROE defined by D'Amico in [12]. It allows the inclusion of the J_2 effects as well as those due to the external accelerations. Finally, the acceleration control profile used in this work is presented.

A. Relative Dynamics Model

The relative motion of a spacecraft (deputy) with respect to another one, referred to as chief, can be parameterized using the dimensionless relative orbit elements defined by [12]

$$\delta\boldsymbol{\alpha}\begin{bmatrix} a_d/a_c - 1 \\ (u_d - u_c) + (\Omega_d - \Omega_c)c_{(i_c)} \\ e_{xd} - e_{xc} \\ e_{yd} - e_{yc} \\ i_d - i_c \\ (\Omega_d - \Omega_c)s_{(i_c)} \end{bmatrix} = \begin{bmatrix} \delta a \\ \delta\lambda \\ \delta e_x \\ \delta e_y \\ \delta i_x \\ \delta i_y \end{bmatrix} \in \mathbb{R}^6 \quad (1)$$

where a, i, Ω, and u indicate the semimajor axis, inclination, right ascension of the ascending node, and argument of latitude. The symbols $s_{(\cdot)}$ and $c_{(\cdot)}$ denote the functions $\sin(\cdot)$ and $\cos(\cdot)$, respectively. The terms e_x and e_y represent the components of eccentricity vector and are defined as $e_x = e\cos(\omega)$ and $e_x = e\cos(\omega)$, where e and ω are the orbit eccentricity and the argument of perigee, respectively. In Eq. (1), the subscripts c and d label the chief and deputy satellite. Then, the relative state vector $\delta\boldsymbol{\alpha}$ consists of the relative semimajor axis δa the relative longitude $\delta\lambda$ as well as the coordinates of the relative eccentricity vector δe and relative inclination vector δi, respectively. The preceding relative state is nonsingular for circular orbits ($e_c = 0$), whereas it is still singular for strictly equatorial orbits ($i_c = 0$) [3].

The averaging theory [13] can be used to derive the variation of the mean ROE due to the Earth's oblateness J_2 [7,14]. Moreover, as discussed by the authors in [7], the well-known GVE [5] can be exploited to determine the change of the mean ROE due to the continuous control acceleration $\boldsymbol{f}(t) \in \mathbb{R}^3$. Hence, the set of nonlinear differential equations describing the mean relative motion under the effects of J_2 perturbing acceleration and the continuous control acceleration acting on the deputy can be written as follows [7]:

$$\delta\dot{\boldsymbol{\alpha}}\begin{bmatrix} \mathbf{0} \\ n_d(\boldsymbol{\alpha}_c, \boldsymbol{\alpha}_d) - n_c(\boldsymbol{\alpha}_c) \\ \mathbf{0}_{4\times 1} \end{bmatrix} + \boldsymbol{\sigma}_{J_2}(\boldsymbol{\alpha}_c, \boldsymbol{\alpha}_d) + \boldsymbol{\sigma}_F(\boldsymbol{\alpha}_c, \boldsymbol{\alpha}_d, \boldsymbol{f}(t))$$
$$= \boldsymbol{\xi}(\boldsymbol{\alpha}_c, \boldsymbol{\alpha}_d, \boldsymbol{f}(t)) \quad (2)$$

where

$$\boldsymbol{\sigma}_{J_2}(\boldsymbol{\alpha}_c, \boldsymbol{\alpha}_d)$$
$$= \begin{bmatrix} 0 \\ (\eta_d P_d K_d - \eta_c P_c K_c) + (K_d Q_d - K_c Q_c) - 2(K_d c_{i_d} - K_c c_{i_c})c_{(i_c)} \\ -e_{yd}K_d Q_d + e_{yc}K_c Q_c \\ e_{xd}K_d Q_d - e_{yc}K_c Q_c \\ 0 \\ -2(K_d c_{(i_d)} - K_c c_{(i_c)})s_{(i_c)} \end{bmatrix}$$
$$(3)$$

$$\boldsymbol{\sigma}_F(\boldsymbol{\alpha}_c, \boldsymbol{\alpha}_d, \boldsymbol{f}(t)) = \begin{bmatrix} \frac{\dot{a}_d}{a_c} \\ \dot{u}_d + \dot{\Omega}_d c_{(i_c)} \\ \dot{e}_{xd} \\ \dot{e}_{yd} \\ i_d \\ \dot{\Omega}_d s_{(i_c)} \end{bmatrix} = \boldsymbol{\Gamma}_F(\boldsymbol{\alpha}_d)\boldsymbol{f}(t) \quad (4)$$

The vector $\boldsymbol{\alpha}_{(\cdot)}$, where the subscript $(\cdot)$ stands for c and d, denotes the quasi-nonsingular orbital elements vector, i.e., $\boldsymbol{\alpha}_{(\cdot)} = [a_{(\cdot)}, e_{x(\cdot)}, e_{y(\cdot)}, i_{(\cdot)}, \Omega_{(\cdot)}, u_{(\cdot)}]^T$, where $e_{x(\cdot)} = e_{(\cdot)}\cos(\omega_{(\cdot)})$, $e_{y(\cdot)} = e_{(\cdot)}\sin(\omega_{(\cdot)})$, and $u_{(\cdot)} = M_{(\cdot)} + \omega_{(\cdot)}$. In Eq. (3), the quantities $K_{(\cdot)}$, $Q_{(\cdot)}$, $P_{(\cdot)}$, and $\eta_{(\cdot)}$ are

$$K_{(\cdot)} = \frac{\gamma n_{(\cdot)}}{a_{(\cdot)}^2 \eta_{(\cdot)}^4} \qquad \eta_{(\cdot)} = \sqrt{1 - e_{(\cdot)}^2} \qquad n_{(\cdot)} = \sqrt{\frac{\mu_\oplus}{a_{(\cdot)}^3}}$$
$$Q_{(\cdot)} = 5\cos(i_{(\cdot)})^2 - 1 \quad P_{(\cdot)} = 3\cos(i_{(\cdot)})^2 - 1 \quad \gamma = \tfrac{3}{4}J_2 R_E^2$$
$$(5)$$

where J_2 indicates the second spherical harmonic of the Earth's geopotential ($J_2 = 1.082 \times 10^{-3}$), R_E is the Earth's equatorial radius ($R_E = 6378.13$ km), and $\mu_\oplus$ is the Earth gravitational parameter ($\mu_\oplus = 3.98600 \times 10^5$ km^3/s^2). The individual terms of the control influence matrix $\mathbf{\Gamma}_F(\boldsymbol{\alpha}_d)$ in Eq. (4) are listed in the Appendix. Note that the function $\boldsymbol{\xi}(\boldsymbol{\alpha}_c, \boldsymbol{\alpha}_d, \boldsymbol{f}(t))$ can be reformulated in terms of $\boldsymbol{\alpha}_c$ and $\delta\boldsymbol{\alpha}$ using the following identities [14]:

$$a_d = a_c\delta a + a_c \qquad e_d = \sqrt{(e_{xc} + \delta e_x)^2 + (e_{yc} + \delta e_y)^2}$$

$$i_d = i_c + \delta i_x \qquad \omega_d = \tan^{-1}\left(\frac{e_{yc} + \delta e_y}{e_{xc} + \delta e_x}\right)$$

$$\Omega_d = \Omega_c + \frac{\delta i_y}{\sin(i_c)} \qquad u_d = u_c + \delta\lambda + (\Omega_d - \Omega_c)\cos(i_c) \qquad (6)$$

Performing a first-order Taylor expansion of the nonlinear function $\boldsymbol{\xi}(\boldsymbol{\alpha}_c, \delta\boldsymbol{\alpha}, \boldsymbol{f}(t))$ in Eq. (2) around the chief orbit (i.e., $\delta\boldsymbol{\alpha} = \mathbf{0}$ and $\boldsymbol{f} = \mathbf{0}$) and assuming that the chief is moving on a near-circular orbit (i.e. $e_c \to 0$) yield the following linear dynamics model [7]:

$$\delta\dot{\boldsymbol{\alpha}}(t) = \frac{\partial\boldsymbol{\xi}}{\partial\delta\boldsymbol{\alpha}}\bigg]_{\substack{\delta\alpha=0 \\ f=0}}\delta\boldsymbol{\alpha}(t) + \frac{\partial\boldsymbol{\xi}}{\partial\boldsymbol{f}}\bigg]_{\substack{\delta\alpha=0 \\ f=0}}\boldsymbol{f} = A_{\text{NC}}\delta\boldsymbol{\alpha}(t) + \boldsymbol{B}_{\text{NC}}(t)\boldsymbol{f}(t) \qquad (7)$$

where $A_{\text{NC}} \in \mathbb{R}^{6\times6}$ and $\boldsymbol{B}_{\text{NC}} \in \mathbb{R}^{6\times3}$ are the plant matrix and input sensitivity matrix related to the control acceleration $\boldsymbol{f}(t) \in \mathbb{R}^3$, respectively, here reported for completeness:

$$A_{\text{NC}} = \begin{bmatrix} 0 & 0 & 0 & 0 & 0 & 0 \\ -\Lambda_c & 0 & 0 & 0 & -K_cF_cS_c & 0 \\ 0 & 0 & 0 & -K_cQ_c & 0 & 0 \\ 0 & 0 & K_cQ_c & 0 & 0 & 0 \\ 0 & 0 & 0 & 0 & 0 & 0 \\ \frac{7K_cS_c}{2} & 0 & 0 & 0 & 2K_cT_c & 0 \end{bmatrix}$$

$$\boldsymbol{B}_{\text{NC}}(u_c) = \frac{1}{n_ca_c}\begin{bmatrix} 0 & 2 & 0 \\ -2 & 0 & 0 \\ s_{(u_c)} & 2c_{(u_c)} & 0 \\ -c_{(u_c)} & 2s_{(u_c)} & 0 \\ 0 & 0 & c_{(u_c)} \\ 0 & 0 & s_{(u_c)} \end{bmatrix} \qquad (8)$$

In Eq. (8), the following substitutions are applied for clarity:

$$F_c = 4 + 3\eta_c, \qquad E_c = 1 + \eta_c, \qquad S_c = \sin(2i_c),$$

$$T_c = \sin(i_c)^2, \qquad \Lambda_c = \frac{3}{2}n_c + \frac{7}{2}E_cK_cP_c \qquad (9)$$

The term u_c indicates the mean argument of latitude of the chief orbit at the instant t and is related to the time t through the following expression:

$$u_c = u_0 + W_c(t - t_0) \qquad (10)$$

where $W_c = n_c + K_cQ_c + \eta_cK_cP_c$, and $u_0 = u_c(t_0)$ [7]. Note that the variables t and u_c can be considered interchangeable because they are linearly related through Eq. (10). As discussed in [7,14,15], the complete solution of the system of differential equations [Eqs. (7) and (8)] is given by

$$\delta\boldsymbol{\alpha}(u_c) = \boldsymbol{\Phi}_{\text{NC}}(u_c, u_0)\delta\boldsymbol{\alpha}_0 + \boldsymbol{\Psi}_{\text{NC}}(u_c, u_0)\boldsymbol{f}(u_c) \qquad (11)$$

where $\delta\boldsymbol{\alpha}_0 = \delta\boldsymbol{\alpha}(u_0)$ is the mean ROE at the initial instant t_0, $\boldsymbol{f}(u_c) \in \mathbb{R}^3$ is a continuous piecewise constant function (see Sec. II.B for more details), and $\boldsymbol{\Phi}_{\text{NC}}(u_c, u_0) \in \mathbb{R}^{6\times6}$ and $\boldsymbol{\Psi}_{\text{NC}}(u_c, u_0) \in \mathbb{R}^{6\times3}$ are the state transition matrix and the convolution matrix, respectively, i.e.,

$$\boldsymbol{\Phi}_{\text{NC}}(u_c, u_0) = \begin{bmatrix} 1 & 0 & 0 & 0 & 0 & 0 \\ -\Lambda_c\frac{\Delta u}{W_c} & 1 & 0 & 0 & -K_cF_cS_c\frac{\Delta u}{W_c} & 0 \\ 0 & 0 & c_{(C\Delta u)} & -s_{(C\Delta u)} & 0 & 0 \\ 0 & 0 & s_{(C\Delta u)} & c_{(C\Delta u)} & 0 & 0 \\ 0 & 0 & 0 & 0 & 1 & 0 \\ \frac{7}{2}K_cS_c\frac{\Delta u}{W_c} & 0 & 0 & 0 & 2K_cT_c\frac{\Delta u}{W_c} & 1 \end{bmatrix} \qquad (12)$$

$$\boldsymbol{\Psi}_{\text{NC}}(u_c, u_0)$$
$$= \begin{bmatrix} 0 & \frac{2\Delta u}{n_ca_cW_c} & 0 \\ -\frac{2\Delta u}{n_ca_cW_c} & -\frac{\Lambda_c\Delta u^2}{n_ca_cW_c^2} & \frac{F_cK_cS_c(c_{(u_c)}-c_{(u_0)})+s_{(u_0)}\Delta u)}{n_ca_cW_c^2} \\ -\frac{c_{(u_c)}-c_{(u_0+C\Delta u)}}{n_ca_c\beta W_c} & 2\frac{s_{u_c}-s_{(u_0+C\Delta u)}}{n_ca_c\beta W_c} & 0 \\ -\frac{s_{(u_c)}-s_{(u_0+C\Delta u)}}{n_ca_c\beta W_c} & -2\frac{c_{u_c}-c_{(u_0+C\Delta u)}}{n_ca_c\beta W_c} & 0 \\ 0 & 0 & \frac{s_{(u_c)}-s_{(u_0)}}{n_ca_cW_c} \\ 0 & \frac{7}{2}\frac{K_cS_c\Delta u^2}{n_ca_cW_c^2} & \begin{pmatrix} -\frac{(W_c+2K_cT_c)(c_{(u_c)}-c_{(u_0)})}{n_ca_cW_c^2} \\ -\frac{2K_cT_cs_{(u_0)}\Delta u}{n_ca_cW_c^2} \end{pmatrix} \end{bmatrix} \qquad (13)$$

In Eqs. (12) and (13), Δu indicates the variation of the mean argument of latitude of the chief orbit between the instant t_0 and t (i.e., $\Delta u = u_c - u_0$). The quantities C and β are constant coefficients that depend on the mean semimajor axis, mean eccentricity, and inclination of the chief orbit as follows [7,15]:

$$C = \frac{(K_cQ_c)}{W_c}, \qquad \beta = 1 - C \qquad (14)$$

B. Piecewise Constant Control Profile

In this study, only the deputy is assumed to be maneuverable and capable of providing a thrust along the x, y, and z directions of its own radial–tangential–normal (RTN) reference frame. This reference frame consists of a basis vector with x directed along the absolute position vector, z along the angular momentum of the orbit, and y completing the right-handed orthonormal basis. The control acceleration profile is to be a piecewise constant function $\boldsymbol{f}(u_c) = [f_x(u_c), f_y(u_c), f_z(u_c)]^T \in \mathbb{R}^3$ defined in the maneuvering interval $[u_0, u_T]$ ($u_T = u_c(t = T)$) as (see Fig. 1)
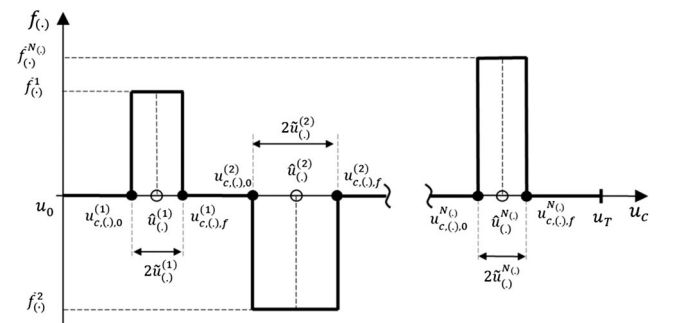

Fig. 1 Piecewise constant acceleration profile for a generic axis (·) of RTN reference frame.

$$f_{(\cdot)}(u_c) = \begin{cases} \bar{f}_{(\cdot)}^{(j)} = \text{const} \neq 0, & u_{c(\cdot),0}^{(j)} \leq u_c \leq u_{c(\cdot),f}^{(j)}, \quad \bar{f}_{(\cdot),j} \in \mathbb{R}, \quad j = 1, \dots, N_{(\cdot)} \\ 0, & \text{otherwise} \end{cases} \tag{15}$$

The term $N_{(\cdot)} \in \mathbb{N}$ denotes the number of finite-time maneuvers along the axis $(\cdot)$ within the interval $[u_0, u_T]$, whereas $u_{c(\cdot),0}^{(j)}$ and $u_{c(\cdot),f}^{(j)}$ indicate the mean argument of latitude of the chief orbit at the beginning and the end of the jth maneuver, respectively, or alternately the initial and final instant of time of the jth maneuver according to the relationship reported in Eq. (10).

By assuming that the relative motion is well described by the linear model [Eqs. (7) and (8)] with the closed-form solution reported in Eqs. (11–13) and that the control acceleration has the form described in Eq. (15), the total change of the mean ROE through the maneuvering interval, $\Delta\delta\boldsymbol{\alpha}(u_T) = \delta\boldsymbol{\alpha}(u_T) - \boldsymbol{\Phi}(u_T, u_0)\delta\boldsymbol{\alpha}_0$, can be analytically computed as follows [7]:

$$\Delta\delta\boldsymbol{\alpha}(u_T) = \boldsymbol{\varrho}_x(u_T) + \boldsymbol{\varrho}_y(u_T) + \boldsymbol{\varrho}_z(u_T) \tag{16}$$

where

$$\boldsymbol{\varrho}_x(u_T) = \sum_{j=1}^{N_x}\left(\boldsymbol{\Phi}\left(u_T, u_{cx,f}^{(j)}\right)\boldsymbol{\Psi}\left(u_{cx,f}^{(j)}, u_{cx,0}^{(j)}\right)\begin{bmatrix} \bar{f}_x^{(j)} \\ 0 \\ 0 \end{bmatrix}\right) \tag{17}$$

$$\boldsymbol{\varrho}_y(u_T) = \sum_{j=1}^{N_y}\left(\boldsymbol{\Phi}\left(u_T, u_{cy,f}^{(j)}\right)\boldsymbol{\Psi}\left(u_{cy,f}^{(j)}, u_{cy,0}^{(j)}\right)\begin{bmatrix} 0 \\ \bar{f}_y^{(j)} \\ 0 \end{bmatrix}\right) \tag{18}$$

$$\boldsymbol{\varrho}_z(u_T) = \sum_{j=1}^{N_z}\left(\boldsymbol{\Phi}\left(u_T, u_{cz,f}^{(j)}\right)\boldsymbol{\Psi}\left(u_{cz,f}^{(j)}, u_{cz,0}^{(j)}\right)\begin{bmatrix} 0 \\ 0 \\ \bar{f}_z^{(j)} \end{bmatrix}\right) \tag{19}$$

In further detail, Eqs. (16–19) can be written in the extended form as follows:

$$\sum_{j=1}^{N_y} \tilde{u}_y^{(j)} \bar{f}_y^{(j)} = \kappa\Delta\delta a(u_T) \tag{20}$$

$$\sum_{j=1}^{N_x} \tilde{u}_x^{(j)} \bar{f}_x^{(j)} + \frac{\Lambda_c}{W_c}\sum_{j=1}^{N_y}\left(u_T - \hat{u}_y^{(j)}\right)\tilde{u}_y^{(j)} \bar{f}_y^{(j)} +$$
$$- \frac{F_c K_c S_c}{2W_c}\sum_{j=1}^{N_z}\left(-s_{(\hat{u}_z^{(j)})}s_{(\tilde{u}_z^{(j)})} + s_{(\hat{u}_z^{(j)} - \tilde{u}_z^{(j)})}\tilde{u}_z^{(j)}\right.$$
$$\left. - \left(u_T - \hat{u}_z^{(j)} - \tilde{u}_z^{(j)}\right)c_{(\hat{u}_z^{(j)})}s_{(\tilde{u}_z^{(j)})}\right)\bar{f}_z^{(j)} = -\kappa\Delta\delta\lambda(u_T) \tag{21}$$

$$\frac{1}{2\beta}\sum_{j=1}^{N_x} s_{(Cu_T + \beta\hat{u}_x^{(j)})}s_{(\beta\tilde{u}_x^{(j)})}\bar{f}_x^{(j)} + \frac{1}{\beta}\sum_{j=1}^{N_y} c_{(Cu_T + \beta\hat{u}_y^{(j)})}s_{(\beta\tilde{u}_y^{(j)})}\bar{f}_y^{(j)}$$
$$= \kappa\Delta\delta e_x(u_T) \tag{22}$$

$$-\frac{1}{2\beta}\sum_{j=1}^{N_x} c_{(Cu_T + \beta\hat{u}_x^{(j)})}s_{(\beta\tilde{u}_x^{(j)})}\bar{f}_x^{(j)} + \frac{1}{\beta}\sum_{j=1}^{N_y} s_{(Cu_T + \beta\hat{u}_y^{(j)})}s_{(\beta\tilde{u}_y^{(j)})}\bar{f}_y^{(j)}$$
$$= \kappa\Delta\delta e_y(u_T) \tag{23}$$

$$\frac{1}{2}\sum_{j=1}^{N_z} c_{(\hat{u}_z^{(j)})}s_{(\tilde{u}_z^{(j)})}\bar{f}_z^{(j)} = \kappa\Delta\delta i_x(u_T) \tag{24}$$

$$\frac{7K_c S_c}{2W_c}\sum_{j=1}^{N_y}\left(u_T - \hat{u}_y^{(j)}\right)\tilde{u}_y^{(j)} \bar{f}_y^{(j)}$$
$$+ \frac{1}{W_c}\sum_{j=1}^{N_z}\left(K_c T_c\left(u_T - \hat{u}_z^{(j)} - \tilde{u}_z^{(j)}\right)c_{(\hat{u}_z^{(j)})}s_{(\tilde{u}_z^{(j)})}\right.$$
$$\left. + \frac{1}{2}(W_c + 2K_c T_c)s_{(\hat{u}_z^{(j)})}s_{(\tilde{u}_z^{(j)})} - K_c T_c s_{(\hat{u}_z^{(j)} - \tilde{u}_{z,j})}\tilde{u}_z^{(j)}\right)\bar{f}_z^{(j)}$$
$$= \kappa\Delta\delta i_y(u_T) \tag{25}$$

where $\kappa = W_c n_c a_c/4$. $\tilde{u}_{(\cdot)}^{(j)}$ and $\hat{u}_{(\cdot)}^{(j)}$ indicate the half angular duration and the angular location of the center of the jth finite-time maneuver, respectively, i.e.,

$$\tilde{u}_{(\cdot)}^{(j)} = \frac{u_{c(\cdot),f}^{(j)} - u_{c(\cdot),0}^{(j)}}{2}, \qquad \hat{u}_{(\cdot)}^{(j)} = \frac{u_{c(\cdot),f}^{(j)} + u_{c(\cdot),0}^{(j)}}{2} \tag{26}$$

From Eqs. (20–25), it is clear that the variation of the mean ROE at the end of the maneuvering interval, $\Delta\delta\boldsymbol{\alpha}(u_T) = [\Delta\delta a(u_T), \Delta\delta\lambda(u_T), \Delta\delta e_x(u_T), \Delta\delta e_y(u_T), \Delta\delta i_x(u_T), \Delta\delta i_y(u_T)]^T$, is a nonlinear function of $\hat{u}_{(\cdot)}^{(j)}$ and $\tilde{u}_{(\cdot)}^{(j)}$, whereas it depends linearly on the acceleration amplitudes $f_{(\cdot)}^{(j)}$. Moreover, it is worth noting that, because of J_2 perturbation, the in-plane and out-of-plane dynamics are coupled [see Eq. (8)]. Then, the control accelerations along the cross-track and along-track directions, $f_z^{(j)}$ and $f_y^{(j)}$, will affect also the mean relative longitude and y component of the relative inclination vector, respectively [see Eqs. (21) and (26)].

C. Fuel-Optimal Reconfiguration Maneuvering Problem

The problem of designing the fuel-minimum maneuver for the formation reconfiguration can be formulated as a Lagrange optimal control problem [16] with the performance index

$$J = \int_{u_0}^{u_T} |f_x(u_c)|\, du_c + \int_{u_0}^{u_T} |f_y(u_c)|\, du_c + \int_{u_0}^{u_T} |f_z(u_c)|\, du_c \tag{27}$$

Hence, the optimization problem can be summarized as follows:

Find $\boldsymbol{f}(u_c): u_c \to \mathcal{F} \subset \mathbb{R}^3, \quad u_c \in \mathbb{R}$

minimizing J

subject to $\quad \forall \, u_c \in [u_0, u_T]$

dynamics constraints: $\delta\dot{\boldsymbol{\alpha}}(u_c) = \boldsymbol{A}_{\mathrm{NC}}\delta\boldsymbol{\alpha}(u_c) + \boldsymbol{B}_{\mathrm{NC}}(u_c)\boldsymbol{f}(u_c)$

boundary constraints: $\delta\boldsymbol{\alpha}(u_T) = \delta\boldsymbol{\alpha}_{\mathrm{des}}$

(or alternately, $\Delta\delta\boldsymbol{\alpha}(u_T) = \Delta\delta\boldsymbol{\alpha}_{\mathrm{des}}$)

path constraints: $\quad \boldsymbol{x}(\delta\boldsymbol{\alpha}(u_c)) > \boldsymbol{x}_{ca}$

control constraints: $\quad f^{\min} \leq |f_{(\cdot)}(u_c)| \leq f^{\max} \quad f^{\max}, f^{\min} > 0 \in \mathbb{R}$
$$\tag{28}$$

The dynamics constraints have been described in Sec. II.A. The final condition is imposed to guarantee the achievement of the desired

relative configuration $\delta\boldsymbol{\alpha}_{\text{des}}$ in the given maneuvering interval $[u_0, u_T]$. According to Eqs. (16–19), the vector $\delta\boldsymbol{\alpha}(u_T)$ can be computed as

$$\delta\boldsymbol{\alpha}(u_T) = \boldsymbol{\Phi}(u_T, u_0)\delta\boldsymbol{\alpha}_0 + \boldsymbol{\varrho}_x(u_T) + \boldsymbol{\varrho}_y(u_T) + \boldsymbol{\varrho}_z(u_T) \quad (29)$$

During the reconfiguration maneuver, the collision between the satellites has to be prevented. To this purpose, the relative position vector expressed in Cartesian coordinates, $\boldsymbol{x}(\delta\boldsymbol{\alpha}(u_c))$, must lie outside a safety box centered in the chief spacecraft. In this study, the linear mapping originally presented in [17] and discussed more in detail in [18] is used to map the mean ROE vector to the Cartesian relative state, i.e.,

$$\begin{bmatrix} x \\ y \\ \dot{x} \\ \dot{y} \\ z \\ \dot{z} \end{bmatrix} = a_c \boldsymbol{M}(u_c)\delta\boldsymbol{\alpha}(u_c) \quad (30)$$

with

$$\boldsymbol{M}(u_c) = \begin{bmatrix} 1 & 0 & -\cos(u_c) & -\sin(u_c) & 0 & 0 \\ 0 & 1 & 2\sin(u_c) & -2\cos(u_c) & 0 & 0 \\ 0 & 0 & n_c\sin(u_c) & -n_c\cos(u_c) & 0 & 0 \\ -\frac{3}{2}n_c & 0 & 2n_c\cos(u_c) & 2n_c\sin(u_c) & 0 & 0 \\ 0 & 0 & 0 & 0 & \sin(u_c) & -\cos(u_c) \\ 0 & 0 & 0 & 0 & n_c\cos(u_c) & n_c\sin(u_c) \end{bmatrix}$$
$$(31)$$

It is worth remarking that Cartesian relative state should be computed through a series of nonlinear transformations including the relations between Cartesian state and orbital elements [19] and the transformations from osculating to mean elements discussed in [20]. However, because the Jacobian of the osculating-to-mean transformation is approximately a 6x6 identity matrix when J_2 is considered [21], the mean orbit elements can be approximated by the corresponding osculating ones. In addition, when the satellite orbits are near-circular as it is intended in this study, a linear relation mapping the osculating elements to Cartesian state can be used. The preceding considerations justify the use of Eq. (30) to compute the relative Cartesian state directly from the mean ROE vector to the corresponding Cartesian state to allow the inclusion of path constraints through the optimization method proposed in this study.

Finally, because the control form given in Eq. (15), the objective function J in Eq. (28) can be written as follows:

$$J^* = \frac{2}{W_c}\left(\sum_{j=1}^{N_x} |\bar{f}_x^{(j)}|\tilde{u}_x^{(j)} + \sum_{j=1}^{N_y} |\bar{f}_y^{(j)}|\tilde{u}_y^{(j)} + \sum_{j=1}^{N_z} |\bar{f}_z^{(j)}|\tilde{u}_z^{(j)}\right) \quad (32)$$

III. Solution via Mixed-Integer Linear Programming Approach

The optimization problem described by Eq. (28) is nonlinear because of the boundary constraints and the definition of the objective function J^*. In further detail, the variation of the mean ROE at the end of the maneuvering interval u_T is a nonlinear function of the finite-time maneuvers' locations and durations, i.e., $\hat{u}_{(\cdot)}^{(j)}$ and $\tilde{u}_{(\cdot)}^{(j)}$ with $j = 1, \ldots, N_{(\cdot)}$ [see Eqs. (20–25)]. Moreover, the objective function J^* in Eq. (32) is a nonlinear function of the maneuvers' magnitudes $\bar{f}_{(\cdot)}^{(j)}$. Given the specific piecewise constant control profile considered in this study (see Sec. II.B), the optimal control problem [Eq. (28)] can be converted in a constrained NLP problem and, therefore, solved through one of the numerous available algorithms for NLP solution, such as gradient-based algorithms [22], or metaheuristic algorithms

as the genetic or the particle swarm algorithms [23,24]. Nevertheless, the efficiency of the aforementioned algorithms is significantly hindered by the increase of the number of optimization variables. Note that problem (28) is a large-scale NLP problem with, at least $3N_x + 3N_y + 3N_z + 3$ variables: the locations $\hat{u}_{(\cdot)}^{(j)}$, durations $\tilde{u}_{(\cdot)}^{(j)}$, and magnitude $\bar{f}_{(\cdot)}^{(j)}$ of each thruster impulse plus the number of active impulses. In addition, in the NLP problems, the initial guess plays a fundamental role. Starting at a point close to a local optimum might lead the solver to find a local minimum instead of the global one. To overcome these difficulties, the minimum-fuel reconfiguration problem in Eq. (28) is formulated as a MILP problem [25]. The MILP is a generalization of the linear programming (LP) problem [26] in which some variables can be constrained to take only integer values. Constraints on such variables enable the inclusion of logical expressions in the optimization, encoding the combinatorial part of the problem [27]. Therefore, by introducing additional integer variables as well as by discretizing the entire maneuvering interval $[u_0, u_T]$, the problem in Eq. (28) can be fully written in a pure linear form for all the constraints as well as in the objective function. This is discussed in detail in the rest of this section. Once the original optimization problem [Eq. (28)] is converted into the MILP form, numerous software packages can be used for its solution, such as FICO Mosel XPRESS [28], Gurobi [29], or CPLEX [30]. These software packages usually implement linear and/or Lagrangian relaxations embedded in branch-and-bound or brunch-and-cut algorithms, which solve the MILP problem by generating and solving LP subproblems in accordance with a tree search, where the nodes of the tree correspond to LP subproblems [27]. In general, these algorithms are specifically designed to exploit the characteristic linearity of the problem (search of the global optimum within the convex hull of the problem) to be very efficient for large-scale problems, and typically they do not require the definition of an initial guess. Hence, they are the natural choice to solve the problem described in Eq. (28), once written in the linear form. In this study, the CPLEX software package is used. In fact, to the authors' knowledge, it is one of the most efficient and reliable MILP solvers available, implementing the branch-and-bound algorithm in conjunction with many adjustable heuristics.

A. Mixed-Integer Linear Programming Formulation

As mentioned in Sec. III, to make the MILP approach suited for the determination of the minimum-fuel strategy for the formation reconfiguration, the constrained nonlinear optimization problem [Eq. (28)] has to be first transformed into a linear one. To this purpose, let us divide the maneuvering interval $[u_0, u_T]$ in a finite number of subintervals N_d of fixed length $2\tilde{u}_d$ and associate to each of them a finite-time maneuver of magnitude $\boldsymbol{f}^{(m)} = [\bar{f}_x^{(m)}, \bar{f}_y^{(m)}, \bar{f}_z^{(m)}]$, with $\bar{f}_x^{(m)}, \bar{f}_y^{(m)}, \bar{f}_z^{(m)} \in [-f^{\max}, f^{\max}]$ and $m = 1, \ldots, N_d$. In this way, the optimization variables become the maneuvers' magnitudes related to the mth subinterval, $\bar{f}_{(\cdot)}^{(m)}$ (see Fig. 2). However, the discretization of the maneuvering interval does not solve the issue of nonlinearity of
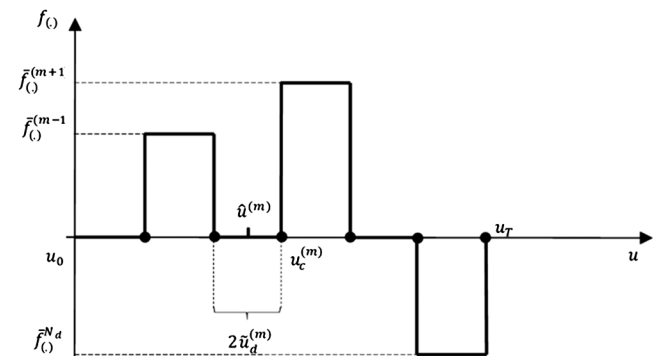

Fig. 2 Example of discretization for a generic axis (·) of RTN reference frame.

the objective function, which would be still nonlinear in $\bar{f}_{(\cdot)}^{(m)}$. Then, let us split $\bar{f}_{(\cdot)}^{(m)}$ into two subsets, $\bar{f}_{(\cdot)}^{+(m)} \in [0, f^{\max}]$ and $\bar{f}_{(\cdot)}^{-(m)} \in [-f^{\max}, 0]$, such that the objective function in Eq. (32) can be rearranged as

$$J^*_{\mathrm{MILP}} = \frac{2}{W_c} \sum_{m=1}^{N_d} \Big[\Big(\bar{f}_x^{+(m)} + \bar{f}_y^{+(m)} + \bar{f}_z^{+(m)} \Big) \tilde{u}_d^{(m)}$$
$$- \Big(\bar{f}_x^{-(m)} + \bar{f}_y^{-(m)} + \bar{f}_z^{-(m)} \Big) \tilde{u}_d^{(m)} \Big] \tag{33}$$

From Eq. (33), the objective function J^*_{MILP} is now a linear function of the new set of optimization variables $[\bar{f}_{(\cdot)}^{+(m)}, \bar{f}_{(\cdot)}^{+(m)}]$, with $m = 1, \ldots, N_d$.

Finally, the MILP problem associated to the minimum-fuel reconfiguration strategy design can be formulated as

$$\text{minimizing} \quad J^*_{\mathrm{MILP}}$$
$$\text{subject to} \quad \forall\, x_{\mathrm{MILP}} = [\eta, \tau]^T, \eta \in \mathbb{R}^{6N_d},$$
$$\tau \in \mathbf{Z} = \{\tau : \tau_s \in \mathbb{N}, s = 1, \ldots, 6N_d\}$$
$$H x_{\mathrm{MILP}} \leq Y \tag{34}$$

where

$$\eta = [f_x^+, f_x^-, f_y^+, f_y^-, f_z^+, f_z^-] \quad \tau = [\rho_x^+, \rho_x^-, \rho_y^+, \rho_y^-, \rho_z^+, \rho_z^-] \tag{35}$$

being

$$f_{(\cdot)}^+ = \Big[\hat{f}_{(\cdot)}^{+(1)}, \ldots, \hat{f}_{(\cdot)}^{+(N_d)} \Big], \qquad f_{(\cdot)}^- = \Big[\hat{f}_{(\cdot)}^{-(1)}, \ldots, \hat{f}_{(\cdot)}^{-(N_d)} \Big]$$
$$\hat{f}_{(\cdot)}^{+(m)} = \frac{\bar{f}_{(\cdot)}^{+(m)}}{f^{\max}} \in \mathbb{R}, \quad \hat{f}_{(\cdot)}^{-(m)} = \frac{\bar{f}_{(\cdot)}^{-(m)}}{f^{\max}} \in \mathbb{R} \tag{36}$$

$$\rho_{(\cdot)}^+ = \Big[\rho_{(\cdot)}^{+(1)}, \ldots, \rho_{(\cdot)}^{+(N_d)} \Big], \quad \rho_{(\cdot)}^- = \Big[\rho_{(\cdot)}^{-(1)}, \ldots, \rho_{(\cdot)}^{-(N_d)} \Big], \quad \rho_{(\cdot)}^{+(m)}, \rho_{(\cdot)}^{-(m)} \in \mathbb{N} \tag{37}$$

Let us recall that the subscript $(\cdot)$ stands for x, y, and z in the preceding expressions. $\hat{f}_{(\cdot)}^{+(m)}$, $\hat{f}_{(\cdot)}^{-(m)}$ are real quantities and express the nondimensional positive and negative control accelerations in the mth interval. They can vary continuously from 0 to 1. $\rho_{(\cdot)}^{+(m)}, \rho_{(\cdot)}^{-(m)}$ are binary variables (integer variables all included in the range $[0, 1]$) introduced to define the sign of the control input along the $(\cdot)$ axis and are defined as follows:

$$\rho_{(\cdot)}^{-(m)} = \begin{cases} 1, & \text{if } \hat{f}_{(\cdot)}^{-(m)} < 0, \\ 0, & \text{otherwise} \end{cases} \quad \rho_{(\cdot)}^{(m)} = \begin{cases} 1, & \text{if } \hat{f}_{(\cdot)}^{-(m)} < 0, \\ 0, & \text{otherwise} \end{cases},$$
$$m = 1, \ldots, N_d \tag{38}$$

According to the optimization problem [Eq. (28)], the following $21N_d$ inequalities have to be included in the MILP formulation [Eq. (34)]:

$$0 \leq \hat{f}_{(\cdot)}^{+(m)} \leq \rho_{(\cdot)}^{+(m)}, \quad 0 \leq \hat{f}_{(\cdot)}^{+(m)} \leq \Big(1 - \rho_{(\cdot)}^{-(m)} \Big), \quad m = 1, \ldots, N_d \tag{39}$$

$$-\rho_{(\cdot),m}^- \leq \hat{f}_{(\cdot)}^{-(m)} \leq 0, \quad -\Big(1 - \rho_{(\cdot)}^{+(m)} \Big) \leq \hat{f}_{(\cdot)}^{-(m)} \leq 0, \quad m = 1, \ldots, N_d \tag{40}$$

$$M_f \Big(\hat{f}_{(\cdot)}^{+(m)} - \hat{f}_{(\cdot)}^{-(m)} \Big) \geq \rho_{(\cdot)}^{+(m)} + \rho_{(\cdot)}^{-(m)}, \quad \text{with } M_f > 0 \in \mathbb{R}, \quad m = 1, \ldots, N_d \tag{41}$$

Equations (39) and (40) are introduced to enforce the definition of quantities $\rho_{(\cdot)}^{+(m)}, \rho_{(\cdot)}^{-(m)}$, i.e., $\hat{f}_{(\cdot)}^{+(m)}$ is different from zero (and positive) only if $\rho_{(\cdot)}^{+(m)}$ is 1 and $\rho_{(\cdot)}^{-(m)}$ is zero, and (vice versa) $\hat{f}_{(\cdot)}^{-(m)}$ is different from zero (and negative) only if $\rho_{(\cdot)}^{-(m)}$ is 1 and $\rho_{(\cdot)}^{+(m)}$ is zero. Finally, Eq. (41) imposes that, for each mth interval, either $\hat{f}_{(\cdot)}^{+(m)}$ or $\hat{f}_{(\cdot)}^{-(m)}$ is different from zero. Thus, in Eq. (33), only one force component, either positive or negative, is considered for each interval. This choice eliminates the nonlinearity given by the absolute value in Eq. (32). Defining $M_f = f^{\max}/f^{\min}$, the magnitudes of the positive and negative finite-time maneuvers, $\bar{f}_{(\cdot)}^{+(m)}$ and $\bar{f}_{(\cdot)}^{-(m)}$, vary in the range $[f^{\min}, f^{\max}]$ and $[-f^{\min}, f^{\max}]$, respectively, with $f^{\min} > 0$. Finally, the equality constraints on the final ROE state [see the boundary constraints in Eq. (28)] are transformed in inequality constraints to match the MILP formulation [Eq. (34)]. More details on the matrix H and the vector Y are given in the following sections. Let us remark that, in accordance to the definition of the MILP state vector reported in Eq. (35), the objective function J^*_{MILP} in Eq. (33) can be rearranged as

$$J^*_{\mathrm{MILP}} = \frac{2f^{\max}}{W_c} \Big[\tilde{u}_d, -\tilde{u}_d, \tilde{u}_d, -\tilde{u}_d, \tilde{u}_d, -\tilde{u}_d, \mathbf{0}_{1 \times 6N_d} \Big] x_{\mathrm{MILP}}$$
$$= \frac{2f^{\max}}{W_c} c x_{\mathrm{MILP}} \tag{42}$$

where $\tilde{u}_d = [\tilde{u}_d^{(1)}, \ldots, \tilde{u}_d^{(N_d)}] \in \mathbb{R}^{N_d}$, and x_{MILP} is defined in Eqs. (34) and (35).

B. Boundary Constraints

At the end of the maneuvering time, u_T, the rth mean ROE component, $\delta\alpha_r(u_T)$, has to be equal to the desired corresponding mean ROE, $\delta\alpha_{r,\mathrm{des}}$, i.e., $\delta\alpha_r(u_T) = \delta\alpha_{r,\mathrm{des}}$, with $r = 1, \ldots, 6$. This equality constraint can be transformed in the following inequalities:

$$(\Delta\delta\alpha_r(u_T) - \Delta\delta\alpha_{r,\mathrm{des}}) \leq \varepsilon_{\mathrm{rel}}|\Delta\delta\alpha_{r,\mathrm{des}}|,$$
$$-(\Delta\delta\alpha_r(u_T) - \Delta\delta\alpha_{r,\mathrm{des}}) \leq \varepsilon_{\mathrm{rel}}|\Delta\delta\alpha_{r,\mathrm{des}}| \tag{43}$$

where $\varepsilon_{\mathrm{rel}}$ is the user-defined tolerance. Hence, Eq. (43) leads to the following 12 inequalities:

$$\pm \frac{f^{\max}}{\kappa} \sum_{m=1}^{N_d} \Big(\hat{f}_y^{+(m)} + \hat{f}_y^{-(m)} \Big) \tilde{u}_d^{(m)} \leq \pm\Delta\delta a_{\mathrm{des}} + \varepsilon_{\mathrm{rel}}|\Delta\delta a_{\mathrm{des}}| \tag{44}$$

$$\pm \frac{f^{\max}}{\kappa} \Bigg(-\sum_{m=1}^{N_d} \Big(\hat{f}_x^{+(m)} + \hat{f}_x^{-(m)} \Big) \tilde{u}_d^{(m)}$$
$$- \frac{\Lambda_c}{W_c} \sum_{m=1}^{N_d} \Big(u_T - \hat{u}^{(m)} \Big) \Big(\hat{f}_y^{+(m)} + \hat{f}_y^{-(m)} \Big) \tilde{u}_d^{(m)}$$
$$+ \frac{F_c K_c S_c}{2W_c} \sum_{m=1}^{N_d} \Big(-\mathrm{s}_{(\hat{u}^{(m)})} \mathrm{s}_{(\tilde{u}_d)} + \mathrm{s}_{(\hat{u}^{(m)} - \tilde{u}_d)} \tilde{u}_d^{(m)}$$
$$- (u_T - \hat{u}^{(m)} - \tilde{u}_d) \mathrm{c}_{(\hat{u}^{(m)})} \mathrm{s}_{(\tilde{u}_d)} \Big) \Big(\hat{f}_z^{+(m)} + \hat{f}_z^{-(m)} \Big) \Bigg)$$
$$\leq \pm\Delta\delta\lambda_{\mathrm{des}} + \varepsilon_{\mathrm{rel}}|\Delta\delta\lambda_{\mathrm{des}}| \tag{45}$$

$$\pm \frac{f^{\max}}{\kappa} \Bigg(\frac{1}{2\beta} \sum_{m=1}^{N_d} \mathrm{s}_{(Cu_T + \beta\hat{u}^{(m)})} \mathrm{s}_{(\beta\tilde{u}_d^{(m)})} \Big(\hat{f}_x^{+(m)} + \hat{f}_x^{-(m)} \Big)$$
$$+ \frac{1}{\beta} \sum_{m=1}^{N_d} \mathrm{c}_{(Cu_T + \beta\hat{u}^{(m)})} \mathrm{s}_{(\beta\tilde{u}_d^{(m)})} \Big(\hat{f}_y^{+(m)} + \hat{f}_y^{-(m)} \Big) \Bigg)$$
$$\leq \pm\Delta\delta e_{x,\mathrm{des}} + \varepsilon_{\mathrm{rel}}|\Delta\delta e_{x,\mathrm{des}}| \tag{46}$$

$$\pm\frac{f^{\max}}{\kappa}\left(-\frac{1}{2\beta}\sum_{m=1}^{N_d}\mathrm{c}_{(Cu_T+\beta\hat{u}^{(m)})}\mathrm{s}_{(\beta\tilde{u}_d^{(m)})}\left(\hat{f}_x^{+(m)}+\hat{f}_x^{-(m)}\right)\right.$$
$$\left.+\frac{1}{\beta}\sum_{m=1}^{N_d}\mathrm{s}_{(Cu_T+\beta\hat{u}^{(m)})}\mathrm{s}_{(\beta\tilde{u}_d^{(m)})}\left(\hat{f}_y^{+(m)}+\hat{f}_y^{-(m)}\right)\right)$$
$$\leq\pm\Delta\delta e_{y,\mathrm{des}}+\varepsilon_{\mathrm{rel}}|\Delta\delta e_{y,\mathrm{des}}| \tag{47}$$

$$\pm\frac{f^{\max}}{\kappa}\left(\frac{1}{2}\sum_{m=1}^{N_d}\mathrm{c}_{(\hat{u}^{(m)})}\mathrm{s}_{(\tilde{u}_d^{(m)})}\left(\hat{f}_z^{+(m)}+\hat{f}_z^{-(m)}\right)\right)$$
$$\leq\pm\Delta\delta i_{x,\mathrm{des}}+\varepsilon_{\mathrm{rel}}|\Delta\delta i_{x,\mathrm{des}}| \tag{48}$$

$$\pm\frac{f^{\max}}{\kappa}\left(\frac{7K_cS_c}{2W_c}\sum_{m=1}^{N_d}(u_T-\hat{u}^{(m)})\left(\hat{f}_y^{+(m)}+\hat{f}_y^{-(m)}\right)\tilde{u}_d^{(m)}\right.$$
$$+\frac{1}{W_c}\sum_{m=1}^{N_d}\left(K_cT_c\left(u_T-\hat{u}^{(m)}-\tilde{u}_d\right)\mathrm{c}_{(\hat{u}^{(m)})}\mathrm{s}_{(\tilde{u}_d)}\right.$$
$$\left.\left.+\frac{1}{2}(W_c+2K_cT_c)\mathrm{s}_{(\hat{u}^{(m)})}\mathrm{s}_{(\tilde{u}_d^{(m)})}-K_cT_c\mathrm{s}_{(\hat{u}^{(m)}-\tilde{u}_d^{(m)})}\tilde{u}_d\right)\left(\hat{f}_z^{+(m)}+\hat{f}_z^{-(m)}\right)\right)$$
$$\leq\pm\Delta\delta i_{y,\mathrm{des}}+\varepsilon_{\mathrm{rel}}|\Delta\delta i_{y,\mathrm{des}}| \tag{49}$$

Note that, in the preceding expressions, the only unknowns are the scaled accelerations' magnitudes $\hat{f}_{(\cdot)}^{+(m)}$ and $\hat{f}_{(\cdot)}^{+(m)}$. In fact, $\hat{u}^{(m)}$ and $\tilde{u}_d^{(m)}$ are not optimization variables because they are established a priori in the discretization process. Therefore, Eqs (44–49) can be expressed in a matricial form as required in Eq. (34). This exercise is left to the reader.

C. Path Constraints

To prevent the collision between the deputy and chief satellites during the reconfiguration maneuver, the deputy vehicle must maintain a specified distance from the chief (i.e., it has to lie outside a specific screening volume around the chief). In this study, a square-base rectangular exclusion zone of dimension R_{ca} is considered. The preceding collision avoidance constraint can be formulated as

$$|x(u_c)-x_{\mathrm{des}}|\geq R_{ca}\ \ \mathrm{OR}\ \ |y(u_c)-y_{\mathrm{des}}|\geq R_{ca}\ \ \mathrm{OR}\ \ |z(u_c)-z_{\mathrm{des}}|\geq R_{ca} \tag{50}$$

where x_{des}, y_{des}, and z_{des} are the Cartesian coordinates of the center of the safety box relative to the chief, and therefore $x_{\mathrm{des}}=y_{\mathrm{des}}=z_{\mathrm{des}}=0$. The constraints in Eq. (50) can be converted into a mixed-integer form by introducing the binary variables $\vartheta_{(\cdot)}^{+(m)}$, $\vartheta_{(\cdot)}^{-(m)}\in[0,1]\in\mathbb{N}$ as follows:

$$-x^{(m)}+x_{\mathrm{des}}\leq-R_{ca}+M_{ca}\vartheta_x^{+(m)},\quad x^{(m)}-x_{\mathrm{des}}\leq-R_{ca}+M_{ca}\vartheta_x^{-(m)},$$
$$m=1,\ldots,N_d \tag{51}$$

$$-y^{(m)}+y_{\mathrm{des}}\leq-R_{ca}+M_{ca}\vartheta_y^{+(m)},\quad y^{(m)}-y_{\mathrm{des}}\leq-R_{ca}+M_{ca}\vartheta_y^{-(m)},$$
$$m=1,\ldots,N_d \tag{52}$$

$$-z^{(m)}+z_{\mathrm{des}}\leq-R_{ca}+M_{ca}\vartheta_z^{+(m)},\quad z^{(m)}-z_{\mathrm{des}}\leq-R_{ca}+M_{ca}\vartheta_z^{-(m)},$$
$$m=1,\ldots,N_d \tag{53}$$

$$\vartheta_x^{+(m)}+\vartheta_x^{-(m)}+\vartheta_y^{+(m)}+\vartheta_y^{-(m)}+\vartheta_z^{+(m)}+\vartheta_z^{-(m)}\leq5,\quad m=1,\ldots,N_d \tag{54}$$

The quantity M_{ca} is an arbitrary positive number, larger than any distance in the problem. The terms $x^{(m)}$, $y^{(m)}$, and $z^{(m)}$ represent the Cartesian coordinates of the deputy position expressed in the chief

RTN reference frame at the mth time instant $u_c^{(m)}=\hat{u}^{(m)}+\tilde{u}_d^{(m)}$ with $m=1,\ldots,N_d$, defined by the maneuvering interval discretization. To be consistent with the MILP formulation, the linear mapping reported in Eq. (30) is employed to determine the Cartesian relative position at $u_c^{(m)}$, i.e.,

$$\begin{bmatrix}x^{(m)}\\y^{(m)}\\\dot{x}^{(m)}\\\dot{y}^{(m)}\\z^{(m)}\\\dot{z}^{(m)}\end{bmatrix}=a_c\boldsymbol{M}(u_c^{(m)})\delta\boldsymbol{\alpha}(u_c^{(m)}) \tag{55}$$

where, according to Eq. (16), $\delta\boldsymbol{\alpha}(u_c^{(m)})$ is

$$\delta\boldsymbol{\alpha}(u_c^{(m)})=\boldsymbol{\varrho}_x(u_c^{(m)})+\boldsymbol{\varrho}_y(u_c^{(m)})+\boldsymbol{\varrho}_z(u_c^{(m)})-\boldsymbol{\Phi}(u_c^{(m)},u_0)\delta\boldsymbol{\alpha}_0 \tag{56}$$

Equations (51–54) are $7N_d$ inequalities to be included in the matrix $\boldsymbol{H}$ [see Eq. (34)]. It is clear that the binary variables $\vartheta_{(\cdot)}^{+(m)}$, $\vartheta_{(\cdot)}^{-(m)}$ have to be added to the optimizer state reported in Eq. (34). Hence, defining the vectors $\boldsymbol{\vartheta}_{(\cdot)}^+=[\vartheta_{(\cdot)}^{(1)},\ldots,\vartheta_{(\cdot)}^{(N_d)}]$ and $\boldsymbol{\vartheta}_{(\cdot)}^-=[\vartheta_{(\cdot)}^{-(1)},\ldots,\vartheta_{(\cdot)}^{-(N_d)}]$, the MILP state becomes $\boldsymbol{x}_{\mathrm{MILP}}=[\boldsymbol{\eta},\boldsymbol{\tau},\boldsymbol{\vartheta}_x^+,\boldsymbol{\vartheta}_x^-,\boldsymbol{\vartheta}_y^+,\boldsymbol{\vartheta}_y^-,\boldsymbol{\vartheta}_z^+,\boldsymbol{\vartheta}_z^-]^T$. Accordingly, the objective function J_{MILP}^* shown in Eq. (42) can be rearranged as $J_{\mathrm{MILP}}^*=(2f^{\max}/W_c)[\boldsymbol{c},0_{1\times6N_d}]\boldsymbol{x}_{\mathrm{MILP}}$.

D. Additional Constraints

The set of constraints discussed in Secs. III.A and III.B, along with those reported in Eqs. (39–41), allows the MILP to solve the optimization problem described in Eq. (28), i.e., to find the minimum-fuel reconfiguration maneuver when an admissible range of acceleration is imposed and an exclusion volume for the relative trajectory is set to prevent the satellites' collision. However, the control profile might be constrained by other practical aspects. From an operational point of view, for instance, the number of finite-time maneuvers to achieve a specific formation configuration cannot be arbitrary. It should be limited to a reasonable number to reduce the complexity of the associated operations and increase the overall reliability. In addition, time constraints might be required to meet technical and operational mission requirements. In this study, the minimum duration of thruster firing and the minimum time spacing between consecutive maneuvers are taken into account. To include the aforementioned constraints, additional binary variables are appended to the MILP state introduced in Sec. III.C, namely and, defined as

$$\sigma^{(m)}=\begin{cases}1,&\text{if }\rho_x^{+(m)}+\rho_x^{-(m)}+\rho_y^{+(m)}+\rho_y^{-(m)}+\rho_z^{+(m)}+\rho_z^{-(m)}\geq1,\\0,&\text{otherwise}\end{cases}$$
$$m=1,\ldots,N_d \tag{57}$$

$$\varsigma^{(m)}=\begin{cases}1,&\text{if }\sum_{k=m}^{m+N_s-1}\sigma^{(k)}=N_s\text{ and }\sigma^{(m-1)}=0,\\0,&\text{otherwise}\end{cases}$$
$$m=2,\ldots,N_d-N_s+1$$

$$\varsigma^{(1)}=\begin{cases}1,&\text{if }\sum_{k=1}^{N_s}\sigma^{(k)}=N_s\\0,&\text{otherwise}\end{cases} \tag{58}$$

The variable $\sigma^{(m)}$ enables one to count the subintervals of time mesh in which the propulsion system delivers the desired acceleration, regardless its direction, whereas the variable $\varsigma^{(m)}$ introduces the concept of RTN maneuver as the consecutive N_s subintervals (i.e., thruster impulses) in which the propulsion system operates. Thus, the parameter N_S [see Eq. (58)] indicates the minimum duration of thrusters' firings. For the sake of clarity, let us
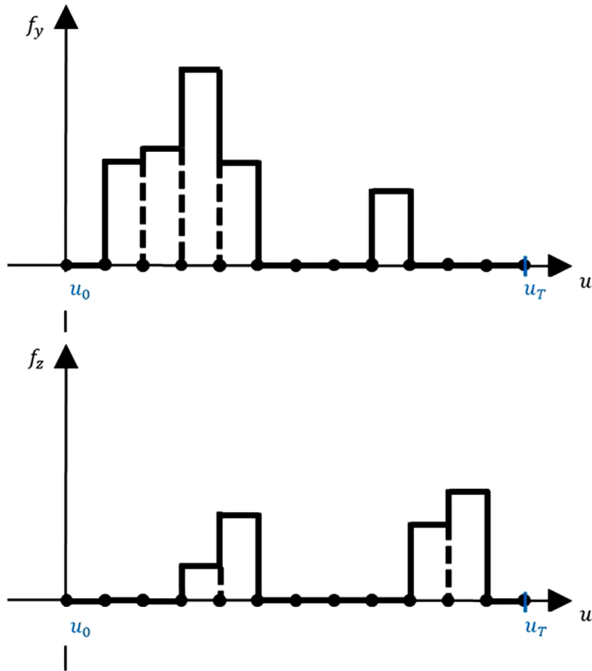
Fig. 3   Example of RTN maneuver.

consider the control profile illustrated in Fig. 3. Accordingly, assuming $N_s = 3$, the vector containing the variable $\sigma^{(m)}$ is $\boldsymbol{\sigma} = [0, 1, 1, 1, 1, 0, 0, 0, 1, 1, 1, 0]$, whereas the vector containing the variable $\varsigma^{(m)}$ is $\boldsymbol{\varsigma} = [0, 1, 0, 0, 0, 0, 0, 0, 1, 0]$. The propulsion system performs two maneuvers.

To obtain a control solution with a maximum number of thruster firings equal to N_I and characterized by a minimum number of consecutive burns of duration $2\tilde{u}_d^{(m)}$ equal to $N_s > 1$, once N_d is set, the following $5N_d - 2N_s + 2$ inequalities are to be included in the MILP formulation:

$$\rho_x^{+^{(m)}} + \rho_x^{-^{(m)}} + \rho_y^{+^{(m)}} + \rho_y^{-^{(m)}} + \rho_z^{+^{(m)}} + \rho_z^{-^{(m)}} \geq \sigma^{(m)}, \quad m = 1, \ldots, N_d \tag{59}$$

$$\rho_x^{+^{(m)}} + \rho_x^{-^{(m)}} + \rho_y^{+^{(m)}} + \rho_y^{-^{(m)}} + \rho_z^{+^{(m)}} + \rho_z^{-^{(m)}} \leq 3\sigma^{(m)}, \quad m = 1, \ldots, N_d \tag{60}$$

$$\varsigma^{(m)} \leq \frac{1}{N_s} \sum_{k=m}^{m+N_s-1} \sigma^{(k)}, \qquad m = 1, \ldots, N_d - N_s + 1 \tag{61}$$

$$\varsigma^{(m)} \leq 1 - \sigma^{(m-1)}, \qquad m = 2, \ldots, N_d - N_s + 1 \tag{62}$$

$$\sigma^{(m)} - \sigma^{(m-1)} \leq \varsigma^{(m)}, \qquad m = 2, \ldots, N_d - N_s + 1 \tag{63}$$

$$\sigma^{(m+1)} \leq \sigma^{(m)}, \qquad m = N_d - N_s, \ldots, N_d - 1 \tag{64}$$

$$\sigma^{(1)} \leq \varsigma^{(1)} \tag{65}$$

$$\sum_{k=1}^{N_d-N_s+1} \varsigma^{(k)} \leq N_I \tag{66}$$

Equations (59–64) enforce the definition of quantities $\sigma^{(m)}$ and $\varsigma^{(m)}$, i.e., $\sigma^{(m)}$ is different from zero only if at least one of the corresponding variables $\rho_{(\cdot)}^{+^{(m)}}$ or $\rho_{(\cdot)}^{-^{(m)}}$ is 1, whereas $\varsigma^{(m)}$ is different from zero only if the sum of consecutive $\sigma^{(m)}$ is equal to N_s and the maneuver starts from the mth element. Equation (66) imposes that the number of thruster firings cannot overcome the value N_I. Ultimately, the constraint on the minimum time separation between consecutive maneuvers can be introduced forcing the thrusters to provide a null acceleration for N_t subintervals. Hence, the following $N_d - N_t$ inequalities are to be added:

$$\sum_{k=m-1}^{\max(m-N_t,1)} \sigma^{(k)} \leq N_t(1 - \varsigma^{(m)}) \quad \text{with } m = 2, \ldots, N_d - N_s + 1 \tag{67}$$

It is worth remarking that the optimizer state vector has to be updated to include the aforementioned additional binary variables $\sigma^{(m)}$ and $\varsigma^{(m)}$. In further detail, the MILP state vector becomes $\boldsymbol{x}_{\text{MILP}} = [\boldsymbol{\eta}, \boldsymbol{\tau}, \boldsymbol{\vartheta}_x^+, \boldsymbol{\vartheta}_x^-, \boldsymbol{\vartheta}_y^+, \boldsymbol{\vartheta}_y^-, \boldsymbol{\vartheta}_z^+, \boldsymbol{\vartheta}_z^-, \boldsymbol{\sigma}, \boldsymbol{\varsigma}]^T$, where $\boldsymbol{\sigma} = [\sigma^{(1)}, \ldots, \sigma^{(N_d)}]$ and $\boldsymbol{\varsigma} = [\varsigma^{(1)}, \ldots, \varsigma^{(N_d-N_s+1)}]$. As a consequence, the objective function J_{MILP}^* in Eq. (42) has to be rearranged as $J_{\text{MILP}}^* = (2f^{\max}/W_c)[\boldsymbol{c}, \boldsymbol{0}_{1\times 6N_d}, \boldsymbol{0}_{1\times N_d}, \boldsymbol{0}_{1\times(N_d-N_s+1)}]\boldsymbol{x}_{\text{MILP}}$, where $\boldsymbol{c} = [\tilde{\boldsymbol{u}}_d, -\tilde{\boldsymbol{u}}_d, \tilde{\boldsymbol{u}}_d, -\tilde{\boldsymbol{u}}_d, \tilde{\boldsymbol{u}}_d, -\tilde{\boldsymbol{u}}_d, \boldsymbol{0}_{1\times 6N_d}]$.

IV.   Numerical Simulations

This section presents the trajectories designed using the MILP formulation, pointing out the maneuvering performances in terms of accuracy and delta-v. A two-satellite formation reconfiguration scenario is considered. Only one of the two spacecraft, namely the deputy, is assumed to be maneuverable and capable of providing continuous thrust along the radial, tangential, and normal directions of its own RTN reference frame. The chief moves on a sun-synchronous circular orbit ($e_c = 0$) with about 98.6 deg inclination at an altitude of 800 km. Without loss of generality, the initial mean right ascension of ascending node and the mean anomaly of the chief orbit are assumed to be zero as well as the mean argument of latitude (i.e., $\Omega_c = M_{c,0} = u_0 = 0$ rad). At the beginning of the maneuver, the mean relative orbit is centered 5 km away from the chief along the along-track direction (i.e., $a_c\delta\lambda = 5$ km). The initial relative inclination vector has a nonzero x component, which corresponds to an inclination difference $\Delta i = 0.0069$ deg. The magnitude and orientation of the initial mean relative inclination vector are $a_c\|\delta\boldsymbol{i}\| = 1.2247$ km and 45 deg, respectively, whereas the magnitude and orientation of the mean relative eccentricity vector are $a_c\delta\boldsymbol{e} = 707.1$ m and -45 deg, respectively. Table 1 reports the initial formation configuration in terms of mean ROE (first row) and the final desired mean relative orbit (second row). It is worth noting that the phases of the desired mean relative eccentricity/inclination vectors do not vary with respect to the initial configuration (i.e., eccentricity/inclination vectors are perpendicular at the beginning and at the end of the reconfiguration maneuver).

To compute the maneuvering accuracy, a high-fidelity satellite orbit simulator is exploited to propagate the initial states of deputy and chief expressed in the Earth-centered inertial (ECI) reference frame (J2000), including 1) the geopotential accelerations determined through the EGM2008 model (up to the 10th order), 2) the atmospheric drag computed through the NRLMSISE-00 density model, 3) the solar radiation pressure perturbation, and 4) the sun and moon gravitational perturbing accelerations. The control acceleration profile obtained in the deputy RTN reference frame is projected in ECI and added as external accelerations to the deputy's motion.

Table 1   Initial and desired mean relative orbits

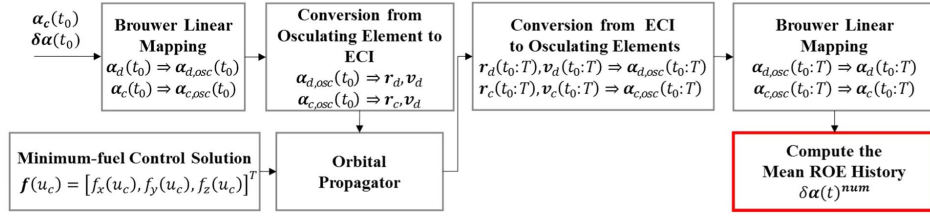| Relative orbit	$a_c\delta a$, m	$a_c\delta\lambda$, m	$a_c\delta e_x$, m	$a_c\delta e_y$, m	$a_c\delta i_x$, m	$a_c\delta i_y$, m
Initial formation configuration	0	5×10^3	500	-500	$500\sqrt{3}$	$500\sqrt{3}$
Desired formation configuration	0	0	800	-800	1600	1600

Fig. 4 Numerical simulations layout.

Note that the linear mapping developed by Brouwer [31] and Lyddane [32] is used to transform the mean orbital elements to osculating and vice versa. As illustrated in Fig. 4, following a chain of transformations comprising the nonlinear relations between Cartesian ECI state and osculating orbital elements and the aforementioned linear map to convert the osculating to mean elements, the distance between the current relative orbit and the desired one can be computed as

$$\epsilon_{\Delta\delta\alpha_r}(t) = \frac{\Delta\delta\alpha_r^{num}(t) - \Delta\delta\alpha_{r,des}}{|\Delta\delta\alpha_{r,des}|} \quad r = 1, \ldots, 6 \quad (68)$$

where $\Delta\delta\boldsymbol{\alpha}^{num}(t) = \delta\boldsymbol{\alpha}^{num}(t) - \boldsymbol{\Phi}(t, t_0)\delta\boldsymbol{\alpha}_0$.

All simulations, including the computation of MILP solution, are carried out using a personal computer with an Intel Core i7-2677M CPU 1.8 GHz processor and 4 GB of RAM.

A. Validation of Mixed-Integer Linear Programming Approach

This section intends to validate the MILP approach presented in Sec. III. To this purpose, the results obtained by the MILP solver are compared with those from the well-known impulsive theory [2,3,12]. In further detail, starting from the scenario described in the previous section, three study cases are investigated, assuming a maneuvering interval of eight chief orbital periods (i.e., $u_T = 16\pi$ rad corresponding to about 13.45 h). First, the unperturbed ($J_2 = 0$) in-plane and out-of-plane reconfiguration problems are considered. The positions of the finite-time burns and the total delta-v obtained through the MILP approach are compared with the corresponding fuel-optimal impulsive solutions discussed by D'Amico [12] and Gaias and D'Amico [2]. Second, the J_2-perturbed full reconfiguration problem is analyzed (i.e., the simultaneous control of the in-plane and out-of-plane relative motion). In this case, the performance of the MILP solution is validated against the fuel-optimal impulsive solution derived by the authors using a particle swarm optimization (PSO) algorithm tailored for the formation control and presented in [15].

Because the lower kinematic efficiency of finite-time maneuvering with respect to the impulsive one, it is expected that the cost of reconfiguration maneuver due to the MILP solution is always higher than the corresponding impulsive one. However, if the discretization is such that the minimum firing duration is small enough with respect to the maneuvering interval, then the location of the finite-time maneuvers has to match (or at least be close to) the position of the impulsive burns.

1. Unperturbed In-Plane Reconfiguration Maneuver

For the in-plane reconfiguration problem in the unperturbed ($J_2 = 0$) circular orbit ($e_c = 0$), it is possible to compute the minimum delta-v required to achieve the desired formation configuration, as discussed in [2,3,33]. This lower delta-v bound is independent from the number or type of executed maneuvers and it is given by [2]

$$V_{LB} = \max\left\{\frac{n_c a_c \Delta\delta e}{2}, \frac{n_c a_c |\Delta\delta a^*|}{2}\right\} \quad (69)$$

where

$$|\Delta\delta a^*| = \max\{|\delta a_{des} - \delta a(u_0)|, |\delta a_{transf}^* - \delta a(u_0)|, |\delta a_{transf}^* - \delta a_{des}|\} \quad (70)$$

and

$$\delta a_{transf}^* = \frac{2}{3}\frac{\Delta\delta\lambda_{des}}{(u_T - u_0)} \quad (71)$$

δa_{transf}^* represents the minimum relative semimajor axis for accomplishing a given mean relative longitude transfer over the finite time to span ($u_T - u_0$). Moreover, from the finding by D'Amico [12] and Gaias and D'Amico [2], if the reconfiguration cost is driven by the variation of relative eccentricity vector, i.e., $\|\Delta\delta e\| > |\Delta\delta a^*|$ and $\|\Delta\delta e\| > 2\Delta\delta\lambda_{des}/3(u_T - u_0)$, the fuel optimal in-plane reconfiguration can be accomplished by three tangential impulses of magnitude

$$\Delta v_{y,imp}^{(j)} = -\frac{n_c a_c \xi_j}{2\pi(k_2(1 - (-1)^{k_3}) - k_3(1 - (-1)^{k_2}))} \quad j = 1, \ldots, 3 \quad (72)$$

located at

$$u_{cy,imp}^{(1)} = \text{atan}\left(\frac{\Delta\delta e_x}{\Delta\delta e_y}\right) + k_1\pi \qquad u_{cy,imp}^{(2)} = u_{cy,imp}^{(1)} + k_2\pi$$

$$u_{cy,imp}^{(3)} = u_{cy,imp}^{(1)} + k_3\pi \quad (73)$$

In Eqs. (72) and (73), $k_j \in \mathbb{N}$, whereas the quantities ξ_j are

$$\xi_1 = (-1)^{k_2}\varphi_1 - (-1)^{k_3}\varphi_2 + (-1)^{k_1}(\chi_2 - \chi_1) \quad (74)$$

$$\xi_2 = \varphi_1 - (-1)^{k_3}\varphi_3 + (-1)^{k_1}\chi_2 \quad (75)$$

$$\xi_3 = \varphi_2 - (-1)^{k_2}\varphi_3 + (-1)^{k_1}\chi_1 \quad (76)$$

$$\varphi_j = \frac{3}{2}n_c(u_T - u_{cy,imp}^{(j)})\Delta\delta a_{des} + n_c\Delta\delta\lambda_{des} \quad (77)$$

$$\chi_1 = \frac{3}{2}n_c k_2\pi\Delta\delta e_{des} \quad \chi_2 = \frac{3}{2}n_c k_3\pi\Delta\delta e_{des} \quad (78)$$

Note that the preceding solution exists if $k_2 \neq k_3$ and if $k_2 = 2n + 1$ (or k_3) when $k_3 = 2n$ (or k_2), with $n \subset \mathbb{N}$.

Let us consider the mission scenario presented in Sec. IV, assuming that only the in-plane components of the mean ROE vector are to be modified by the control strategy, i.e., $a_c\Delta\delta\boldsymbol{\alpha}_{des} = a_c[\Delta\delta a_{des}, \Delta\delta\lambda_{des}, \Delta\delta e_{x,des}, \Delta\delta e_{y,des}]^T = [0, -5 \times 10^3, 300, -300]^T$ m. According to Eq. (69), the lower delta-v bound V_{LB} is 0.2202 m/s. The preceding minimum delta-v can be obtained by the impulsive strategy described by Eqs. (72–77) choosing the parameters $k_1 = 2$, $k_2 = 7$, and $k_3 = 8$. The three tangential impulses have magnitudes $\Delta v_{y,imp}^{(1)} = 0.0826$ m/s, $\Delta v_{y,imp}^{(2)} = -0.11$ m/s, and $\Delta v_{y,imp}^{(3)} = -0.0275$ m/s.

It is worth noting that, because the optimal impulsive scheme described by Eqs. (72) and (73) represents a family of solutions, the lower bound could have been obtained through a different combination of k_j.

To obtain the finite-time maneuver control scheme through the MILP formulation, the "quasi-uniform" time mesh discussed in [15] is employed. This discretization guarantees that the angular separation between the middle point of each finite-time maneuver (i.e., $\hat{u}^{(m)}$) and the reference angle $\bar{u} = \mathrm{atan}(\Delta\delta e_x/\Delta\delta e_y)$ is a multiple of π (i.e., $\tilde{u}_d = d\pi$, where $d \in \mathbb{R}$). This choice guarantees that the impulsive solutions shown in Eqs. (72) and (73) are included in the space of the feasible solution of the optimizer. Let us remind that this discretization is called quasi-uniform because the interval $[u_L, u_R]$ is always uniformly divided in $N_{qu} = N_L + N_R \in \mathbb{N}$ subintervals, with (see [15] for more details)

$$u_R = \bar{u} + \tilde{u}_d + N_R 2\tilde{u}_d, \qquad u_L = \bar{u} + \tilde{u}_d - N_L 2\tilde{u}_d \quad (79)$$

and

$$N_R = \mathrm{floor}\left(\frac{(u_T - (\bar{u} + \tilde{u}_d))}{2\tilde{u}_d}\right), \qquad N_L = \mathrm{floor}\left(\frac{((\bar{u} + \tilde{u}_d) - u_0)}{2\tilde{u}_d}\right) \quad (80)$$

For the simulations presented in this section, it is assumed that $\tilde{u}_d = \pi/16$ rad (i.e., $N_d = 257$), corresponding to a firing duration of 3.152 min. Note that only the boundary constraints are considered here (see Secs. III.A and III.B), i.e., the MILP state vector is $\mathbf{x}_{\mathrm{MILP}} = [\mathbf{f}_x^+, \mathbf{f}_x^-, \boldsymbol{\rho}_x^+, \boldsymbol{\rho}_x^-, \mathbf{f}_y^+, \mathbf{f}_y^-, \boldsymbol{\rho}_y^+, \boldsymbol{\rho}_y^-]^T$. Without loss of generality, the maximum and minimum admissible accelerations are set equal to 0.03 and 3×10^{-5} m/s², respectively.

The MILP approach provides a control solution consisting of three tangential finite-time maneuvers of magnitude $\bar{f}_y^{(1)} = 4.37 \times 10^{-4}$ m/s², $\bar{f}_y^{(2)} = -5.83 \times 10^{-4}$ m/s², and $\bar{f}_y^{(3)} = 1.46 \times 10^{-4}$ m/s² corresponding to $\Delta v_{y,\mathrm{ft}}^{(1)} = -0.082$ m/s, $\Delta v_{y,\mathrm{ft}}^{(2)} = -0.11$ m/s, and $\Delta v_{y,\mathrm{ft}}^{(3)} = 0.0276$ m/s, and a total maneuvering cost of $\Delta v_{\mathrm{Tot,ft}} = |\Delta v_{y,\mathrm{ft}}^{(1)}| + |\Delta v_{y,\mathrm{ft}}^{(2)}| + |\Delta v_{y,\mathrm{ft}}^{(3)}| = 0.02206$ m/s. Figure 5 illustrates the acceleration profile along the tangential direction of the deputy RTN reference frame. Note that the MILP formulation does not produce any maneuver along the radial direction. This result is to be expected due to the higher efficiency of the along-track maneuvers with respect to the radial ones [12]. The middle points of the three tangential finite-time maneuvers are located at the same mean argument of latitude of the impulsive burns, i.e., $\hat{u}_{y,\mathrm{ft}}^{(1)} = u_{y,\mathrm{imp}}^{(1)} = \bar{u} + 2\pi$, $\hat{u}_{y,\mathrm{ft}}^{(2)} = u_{y,\mathrm{imp}}^{(2)} = u_{y,\mathrm{imp}}^{(1)} + 7\pi$, and $\hat{u}_{y,\mathrm{ft}}^{(3)} = u_{y,\mathrm{imp}}^{(3)} = u_{y,\mathrm{imp}}^{(1)} + 8\pi$. The difference of maneuvering cost between the two approaches stems from the dynamics model exploited to derive the finite-time maneuver control strategy (see Sec. II.A). It converges to the impulsive model discussed in [3] when the firing duration $\tilde{u}_d$ tends to zero (i.e., $N_d \to \infty$). For this reason, the MILP solver fires the
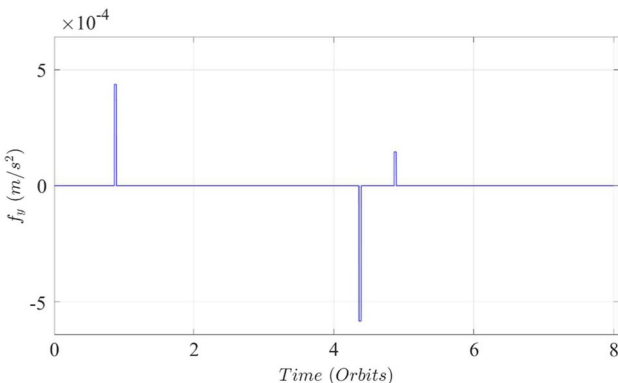
thrusters slightly before and after the optimal instants of time $u_{y,\mathrm{imp}}^{(j)}$, where $j = 1, \ldots 3$, to reduce the total maneuvering delta-v, adjusting the values of $\bar{f}_y^{(j)}$ with $j = 1, \ldots 3$ to get $\Delta v_{y,\mathrm{ft}}^{(j)} \approx \Delta v_{y,\mathrm{imp}}^{(j)}$. In light of this, it is clear that the difference in terms of delta-v between the fuel-optimal impulsive strategy and the one given by the MILP reduces when a finer time mesh is used. A comprehensive analysis of the effects of the discretization on the MILP solution is given in Sec. IV.B.

2. Unperturbed Out-of-Plane Reconfiguration Maneuver

The fuel-optimal impulsive solution for the unperturbed ($J_2 = 0$) circular ($e_c = 0$) out-of-plane reconfiguration problem can be derived analytically and yields [12]

$$\Delta v_{z,\mathrm{imp}}^{(1)} = \frac{n_c a_c}{\cos(u_{z,\mathrm{imp}}^{(1)})} \qquad u_{z,\mathrm{imp}}^{(1)} = \mathrm{atan}\left(\frac{\Delta\delta i_x}{\Delta\delta i_y}\right) + k\pi \quad (81)$$

where $k \in \mathbb{N}$. With reference to the scenario described in Sec. IV and the relative formation configuration summarized in Table 1, the fuel-optimal impulsive solution can be obtained with $k = 0$. Then, the impulsive strategy involves a single burn of magnitude $\Delta v_{z,\mathrm{imp}}^{(1)} = 1.1077$ m/s located at $u_{z,\mathrm{imp}}^{(1)} = 0.78$ rad. Let us recall that only the out-of-plane components of the mean ROE vector have to be modified by the control scheme (i.e., $a_c \Delta\delta\boldsymbol{\alpha}_{\mathrm{des}} = a_c[\Delta\delta i_{x,\mathrm{des}}, \Delta\delta i_{y,\mathrm{des}}]^T = [733.97, 733.97]^T$ m for the simulated maneuver). This means that no in-plane control accelerations are required. In fact, no coupling between the in-plane and out-of-plane dynamics exists because the satellites' orbits are Keplerian.

To derive the MILP solution, the same quasi-uniform discretization introduced in Sec. IV.A.1 is used, with $\bar{u} = \mathrm{atan}(\Delta\delta i_y/\Delta\delta i_x)$ [see Eq. (81)]. In addition, as for the preceding validation simulation, the control acceleration is assumed to range from 3×10^{-5} to 0.03 m/s². Because only the boundary constraints are taken into account, the MILP state vector is further reduced, including $2N_d$ real variables $\mathbf{f}_z^+$ and $\mathbf{f}_z^-$ as well the corresponding $2N_d$ binary variables $\boldsymbol{\rho}_z^+$ and $\boldsymbol{\rho}_z^-$ (i.e., $\mathbf{x}_{\mathrm{MILP}} = [\mathbf{f}_z^+, \mathbf{f}_z^-, \boldsymbol{\rho}_z^+, \boldsymbol{\rho}_z^-]^T$).

Figure 6 depicts the acceleration profile provided by the MILP solver along the cross-track direction of the deputy RTN reference frame. It consists of a single finite-time burn of magnitude $\bar{f}_z^{(1)} = 5.706 \times 10^{-3}$ m/s² whose middle point is located at the same mean argument of latitude of the impulse burn (i.e., $\hat{u}_{z,\mathrm{ft}}^{(1)} = u_{z,\mathrm{imp}}^{(1)} = \bar{u}$). However, the MILP strategy requires higher delta-v (i.e., $\Delta v_{z,\mathrm{ft}}^{(1)} = 1.1079$ m/s). Again, this discrepancy is due to the continuous dynamics model used in the MILP formulation; in fact, when the number of subintervals increases, that is $N_d \to \infty$ and $\tilde{u}_d^{(m)} \to 0$, the continuous dynamics model reduces to the impulsive one; therefore, $\Delta v_{z,\mathrm{ft}}^{(1)} \to \Delta v_{z,\mathrm{imp}}^{(1)}$.

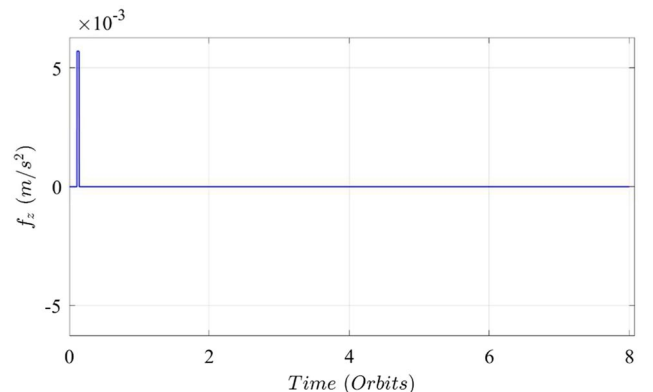**Fig. 5 Along-track acceleration profile obtained by the MILP.**

Fig. 6 Cross-track acceleration profile given by the MILP.

3. J_2-Perturbed Full Reconfiguration Maneuver

In this section, the optimality of the MILP solution for a full reconfiguration maneuver in presence of J_2 perturbation is investigated. The MILP finite-time maneuver control scheme is compared with the fuel-optimal impulsive solution derived using another numerical technique suited for solving nonlinear programming problem, namely the particle swarm optimization (PSO). In fact, to the authors' knowledge, an analytical fuel-optimal impulsive control solution that counts for the coupling due to the J_2 perturbation is not available. The PSO algorithm is a metaheuristic optimization method based on the cooperation between a fixed-size set (swarm) of N_{SW} particles (i.e., a group of candidate solutions containing the optimization parameters [23]). The particles move through the set of acceptable and meaningful solutions, referred to as the feasible search space, modifying their position (i.e., the values of the $\mathcal{M}$ optimization parameters associated with it) through an appropriate perturbation named velocity. During the evolution, the generic ith particle is evaluated at the step k through the performance index J_i^k, which takes into account the goal of the optimization and the imposed constraints [34]. To obtain the impulsive control scheme, the PSO developed by the authors and presented in [15] is employed in this work. With respect to the formulation shown in [15], because an impulsive strategy is to be found, the dynamics model presented in [3] is used. In light of this, the ith PSO particle is defined as follows:

$$x_{i,\mathrm{PSO}} = \left[\Delta v_{x,\mathrm{imp}}, \Delta v_{y,\mathrm{imp}}, \Delta v_{z,\mathrm{imp}}, u_{x,\mathrm{imp}}, u_{y,\mathrm{imp}}, u_{z,\mathrm{imp}} \right]^T$$
$$\in \mathbb{R}^{2N_x + 2N_y + 2N_z} \qquad (82)$$

where

$$\Delta v_{x,\mathrm{imp}} = \left[\Delta v_{x,\mathrm{imp}}^{(1)}, \dots, \Delta v_{x,\mathrm{imp}}^{N_x} \right]^T,$$
$$\Delta v_y = \left[\Delta v_{y,\mathrm{imp}}^{(1)}, \dots, \Delta v_{y,\mathrm{imp}}^{N_y} \right]^T,$$
$$\Delta v_z = \left[\Delta v_{z,\mathrm{imp}}^{(1)}, \dots, \Delta v_{z,\mathrm{imp}}^{N_z} \right]^T \qquad (83)$$

$$u_{x,\mathrm{imp}} = \left[u_{x,\mathrm{imp}}^{(1)}, \dots, u_{x,\mathrm{imp}}^{N_x} \right]^T,$$
$$u_{y,\mathrm{imp}} = \left[u_{y,\mathrm{imp}}^{(1)}, \dots, u_{y,\mathrm{imp}}^{N_y} \right]^T,$$
$$u_{z,\mathrm{imp}} = \left[u_{z,\mathrm{imp}}^{(1)}, \dots, u_{z,\mathrm{imp}}^{N_z} \right]^T \qquad (84)$$

As discussed in [15], the performance index J_i^k includes the total delta-v as well as a penalty function associated to the final condition constraints, i.e.,

$$J_i^k = J^* + \sum_{r=1}^4 d_r \max\left(0, \left| \frac{\Delta \delta \alpha_r(x_{i,\mathrm{PSO}}) - \Delta \delta \alpha_{r,\mathrm{des}}}{\Delta \delta \alpha_{r,\mathrm{des}}} \right| - \varepsilon_{\mathrm{rel}} \right) \quad (85)$$

where J^* is defined in Eq. (32). Note that the PSO approach requires the user to define the maximum number of impulses along each axis to perform the reconfiguration maneuver (i.e., to set the parameters N_x, N_y, and N_z). Here, a maximum number of three impulses along the tangential direction and one along the cross-track direction are chosen. With reference to the orbital scenario presented in Sec. IV, the PSO algorithm leads to a maneuvering cost of 1.2289 m/s, with the magnitudes and locations of the burns reported in Table 2.
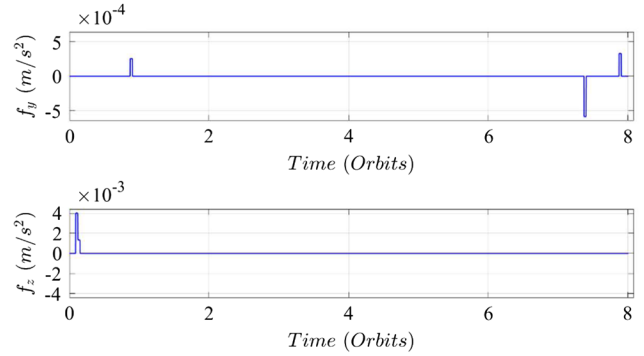
Fig. 7 Along-track and cross-track acceleration profile given by the MILP.

The continuous MILP solution is derived using the quasi-uniform with $\tilde{u}_d = \pi/(16\beta)$ and $\bar{u} = \mathrm{atan}(\Delta \delta i_y / \Delta \delta i_x)/\beta$. The parameter β defined in Eq. (14) is introduced to account for the shift in the impulses' locations due to the J_2 perturbation, as discussed in [15]. This choice leads to a minimum finite-time maneuver of 3.154 min. For this simulation, only the boundary constraints are considered, i.e. $x_{\mathrm{MILP}} = [\eta, \tau]^T$ with η and τ defined in Eq. (35), and the same extreme values of control accelerations used in the preceding validation test cases are imposed. Figure 7 illustrates the control profile obtained by the MILP in the along-track and cross-track directions, which leads to $\Delta v_{\mathrm{Tot}} = 1.2345$ m/s. From the figure, the maneuvers' midpoints are located close to the impulsive burns computed by the PSO algorithm. In further detail, the along-track maneuvers are centered at $\hat{u}_{y,\mathrm{ft}}^{(1)} = 5.5709$ rad, $\hat{u}_{y,\mathrm{ft}}^{(2)} = 46.3884$ rad, and $\hat{u}_{y,\mathrm{ft}}^{(3)} = 49.5282$ rad, whereas the cross-track maneuvers are consecutive and placed at $\hat{u}_{z,\mathrm{ft}}^{(1)} = 0.6650$ rad and $\hat{u}_{z,\mathrm{ft}}^{(2)} = 0.8612$ rad. The slight difference is due to the discretization of the maneuvering interval involved in the MILP formulation. In fact, the finite-time maneuvers can occur only in specific instants depending on the defined time mesh. On the contrary, the impulses computed through the PSO algorithm can be located at any value of u_c.

B. Analysis of Discretization of the Maneuvering Interval

This section aims at investigating the effects of the maneuvering interval discretization on the full reconfiguration strategy performances. To this purpose, a uniform time mesh is considered, with N_d varying between 50 and 700 corresponding to a minimum firing duration ranging between 1.154 and 16.158 min. All simulations presented in the following refer to the scenario presented in Sec. IV, assuming a maneuvering interval of eight chief orbital periods and a control acceleration varying between $f^{\mathrm{min}} = 0.03$ m/s^2 and $f^{\mathrm{max}} = 3 \times 10^{-5}$ m/s^2. In the MILP formulation, both path constraints and additional constraints presented in Secs. III. C and III.D, respectively, are ignored, i.e., $x_{\mathrm{MILP}} = [\eta, \tau]^T$, with η and τ defined in Eq. (35). In fact, when these constraints are included in the formulation, the performance of the control strategy does not depend only on the number of subintervals but rather on the additional user-defined parameters N_I, N_s, and N_t, and on the dimension of the exclusion box R_{ca}.

Figure 8 shows the total maneuvering cost over the number of subintervals. Accordingly, Δv_{Tot} decreases with the increase of N_d. More specifically, the highest value of 1.29 m/s is obtained with the coarsest time mesh (i.e., $N_d = 50$), whereas the smallest value of 1.22 m/s is achieved when the number of subintervals is 666. It is

Table 2 Impulsive PSO solution

Impulses	Tangential Impulses			Cross-track impulses
	Maneuver 1	Maneuver 2	Maneuver 3	Maneuver 1
Locations $u_{(\cdot),\mathrm{imp}}^{(j)}$, rad	5.5255	46.4188	49.5093	0.7140
Magnitude $\Delta v_{(\cdot),\mathrm{imp}}^{(j)}$, m/s	0.0480	−0.1104	0.0624	1.0082

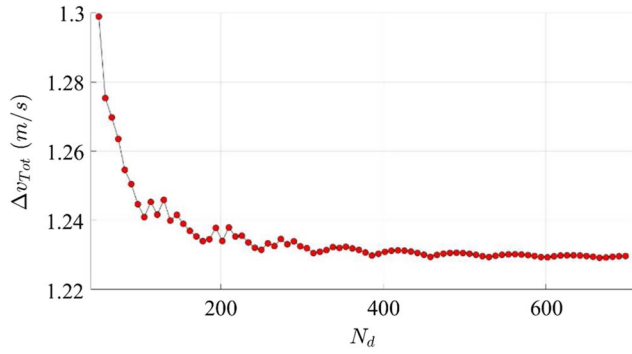Fig. 8　Δv_{Tot} over the number of subintervals.
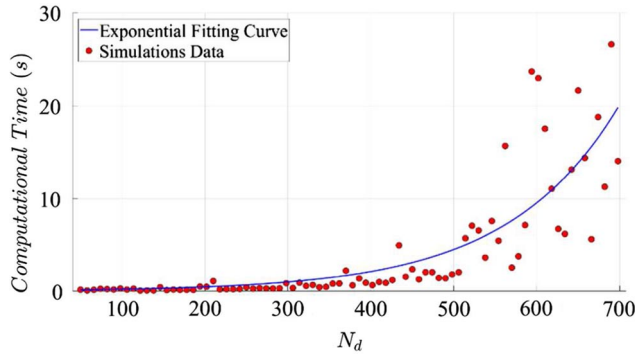
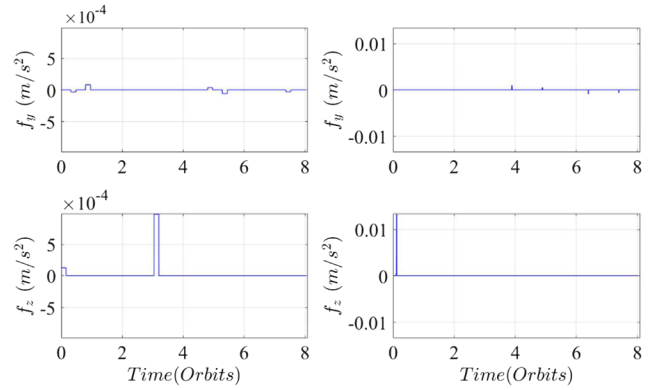Fig. 9　Computing time over the number of subintervals.

Fig. 10　Control profile with $N_d = 50$ (left) and $N_d = 666$ (right).
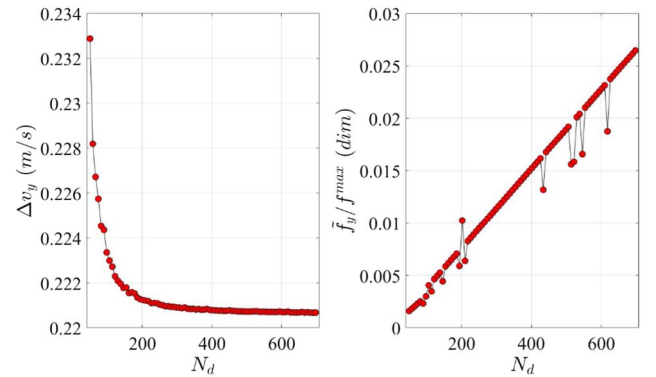

Fig. 11　Velocity (left) and mean values of the maneuvers' amplitude (right) along the y axis over the number of subintervals.
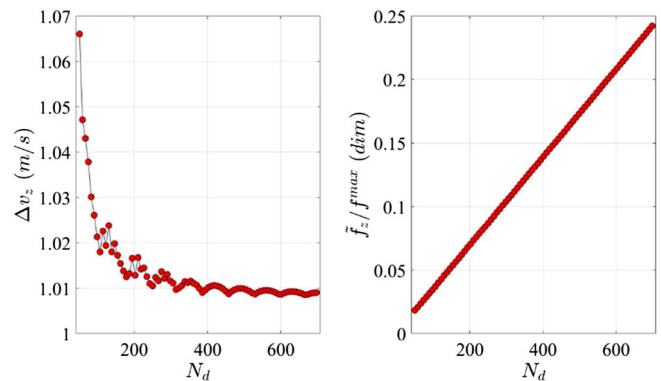

Fig. 12　Velocity (left) and mean values of the maneuvers' amplitude (right) along the z axis over the number of subintervals.

worth remarking that, regardless of the time grid chosen for the MILP implementation, the control acceleration along the radial direction of the deputy RTN reference frame is always null. In addition, for the specific studied case, only an improvement of the total delta-v of 5.42% is achieved with respect to the reference delta-v (i.e., Δv_{Tot} at $N_d = 50$). In further detail, when N_d becomes greater than 210, the gain in term of total delta-v is lower than 0.70% with respect to Δv_{Tot} at $N_d = 210$. Hence, depending on the specific application, a tradeoff should be carried out to evaluate the benefits of a discretization refinement, keeping in mind that the number of variables and inequalities to be handled by the optimizer increases linearly with the parameter N_d (e.g., here the number of variables is $12N_d$ with $21N_d + 12$ inequalities), affecting the computational performance. Figure 9 shows the mean computing time (each dot indicates the average value of computing time determined over 50 runs) versus the number of subintervals N_d. From the figure, the computational performance degrades with the increase of N_d, remaining under 30 s for the specific studied case. In light of this, when the MILP approach is meant to be exploited for onboard determination of the control strategy, an admissible number of subintervals has to be considered. In addition, it must be remarked that the time grid must be compatible (i.e., much larger) with the dynamic response characteristic of the propulsion system and with its capability of reorienting the thrust vector.

Figure 10 illustrates the control profiles corresponding to $N_d = 50$ (left plot) and $N_d = 666$ (right plot). Figure 11 (left) and Fig. 12 (left) depict the variation of delta-v along the y and z axes of the deputy RTN reference frame, respectively, i.e.,

$$\sum_{m}^{N_d} \left| \Delta v_{(\cdot)}^{(m)} \right|$$

where the symbol $(\cdot)$ stands for y and z. Figures 11 and 12 show the evolution of the mean of absolute values of the maneuvers' amplitude over the maneuvering time, i.e.,

$$\tilde{f}_y = \sum_j^{N_y} |\bar{f}_{y,j}|/N_y \quad \text{and} \quad \tilde{f}_z = \sum_j^{N_z} |\bar{f}_{z,j}|/N_z$$

respectively. From these plots, $\tilde{f}_y$ and $\tilde{f}_z$ tend to increase with the increase of the number of discretization intervals. This result is consistent with the fact that the MILP solution tends to the fuel-optimal impulsive one with the increase of N_d, compatibly with the maximum available control acceleration.

C.　Minimum-Fuel Reconfiguration Maneuver Strategy via Mixed-Integer Linear Programming

In this section, the performances of MILP approach in terms of maneuvering delta-v and accuracy are shown. More specifically, three test cases are presented to demonstrate the effectiveness of the constraint formulations discussed in Secs. III.A–III.D. The set of constraints for each test case is listed in Table 3. The last two columns of the table report the number of real/integer variables and the inequalities required to enforce the definition of those variables and impose the constraints discussed in Secs. III.A–III.D. More explicitly, they indicate the dimension of matrix $\boldsymbol{H}$ in Eq. (34). Here, a full reconfiguration maneuver lasting

Table 3   Summary of constraint set for all test cases

Test case	Boundary condition (Sec. III.B)	Path constraint (Sec. III.C)	Additional constraints (Sec. III.D)	Number of variables (real/integer)	Number of inequalities
1	×	——	——	$6N_d/6N_d$	$21N_d + 12$
2	×	×	——	$6N_d/12N_d$	$28N_d + 12$
3	×	×	×	$6N_d/(20N_d - N_s + 1)$	$34N_d - 2N_s - N_t + 14$

16 chief orbital periods is considered, assuming the initial and desired relative configuration summarized in Table 1 (i.e., $a_c \Delta \delta \boldsymbol{\alpha}_{\mathrm{des}} = [0, -5.115 \text{x} 10^3, 329.5, -272.2, 734, 624.7]^T$ m). Note that the effect of J_2 perturbation is taken into account (i.e., the dynamics model described in Sec. II.A is employed to derive the MILP-based control strategy). A uniform time mesh with 240 elements is considered (i.e., a single subinterval lasts 6.73 min). In addition, the magnitude of the acceleration vector is assumed to vary between $f^{\min} = 3 \times 10^{-5}$ m/s² and $f^{\max} = 3 \times 10^{-4}$ m/s². Considering a mass of 100 kg for both spacecraft, the preceding acceleration values are compatible with different classes of low-thrust propulsion system, ranging from Hall-effect propulsion system to radio-frequency ion thrusters [35,36]. Moreover, the deputy onboard thrusters are oriented in such a way to guarantee a thrust along both directions of all axes of RTN reference frame. This assumption entails the duration of subinterval to be compliant with the time response of the thrusters. In fact, the change of direction of the thrust vector is achieved by modulating the amplitude of the control acceleration.

1. Test Case 1

In this scenario, the MILP solution is derived considering only the boundary constraints (see Sec. III.B). In light of this, matrix $\boldsymbol{H}$ in Eq. (34) has the dimension $(21N_d + 12) \times 12N_d$ and includes the inequalities reported in Eqs. (39–41) and Eqs. (51–54), whereazs the optimizer state vector is $\boldsymbol{x}_{\mathrm{MILP}} = [\boldsymbol{\eta}, \boldsymbol{\tau}]^T$, with $\boldsymbol{\eta}$ and $\boldsymbol{\tau}$ defined in Eq. (35). Hence, the formulation involves $6N_d$ binary variables and $6N_d$ real variables.

Figure 13 illustrates the acceleration control profile along y and z directions of the deputy RTN reference frame, consisting of 45 thruster firings. This scheme requires a total delta-v of 1.219 m/s. It is worth mentioning that CPLEX solves the MILP problem in 0.91 s.

Figure 14 shows the mean ROE state variation over the maneuvering interval according to Eq. (68). At the end of the maneuvering interval, the final desired position is achieved with the value of relative accuracies, $\epsilon_{\Delta \delta \alpha_r}(t)$ with $r = 1, \ldots 6$, listed in Table 4. Note that, because the variation of the semimajor axis is null (i.e., $|\Delta \delta a_{\mathrm{des}}| = 0$), the corresponding accuracy $\epsilon_{\Delta \delta a}(T)$ is scaled with respect to $|\Delta \delta e_{x,\mathrm{des}}|$, that is the smallest variation among the ROE components. The total accuracy defined as

$$\epsilon_{\mathrm{Tot}} = a_{c,0} \sqrt{(\epsilon_{\Delta \delta a}(T))^2 + (\epsilon_{\Delta \delta \lambda}(T))^2 + (\epsilon_{\Delta \delta e_x}(T))^2 + (\epsilon_{\Delta \delta e_y}(T))^2 + (\epsilon_{\Delta \delta i_x}(T))^2 + (\epsilon_{\Delta \delta i_y}(T))^2} \qquad (86)$$

is equal to 8.705×10^{-3} m.

Ultimately, Fig. 15 illustrates the evolution of the relative position in the chief RTN reference frame, along with its projection on the x–y plane (Fig. 15a), x–z plane (Fig. 15c), and y–z plane (Fig. 15b). In the figure also the firing intervals are depicted, with the green markers representing the in-plane maneuvers and the cyan ones the cross-track maneuvers. The initial and the desired relative positions are indicated by the red and magenta markers, respectively. It is worth remarking that the phasing characteristics of e/i vectors (see Table 1) does not guarantee a passively safe transfer trajectory, as confirmed by the deputy trajectory shown in Fig. 15d. In this figure, the gray box indicates a 700 m screening volume centered at the chief satellite position. As a consequence, the path constraints have to be included in the MILP formulation to obtain a collision-free maneuvering strategy.
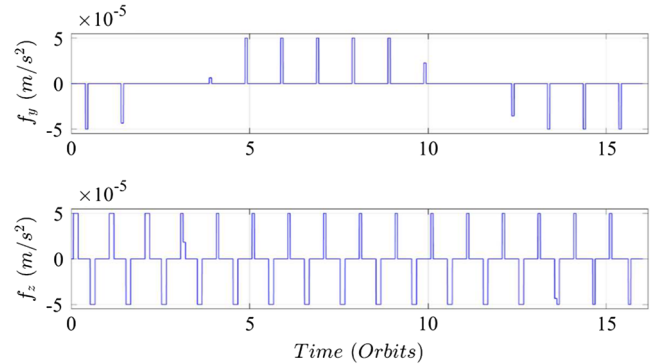
Fig. 13   Acceleration profile for test case 1.
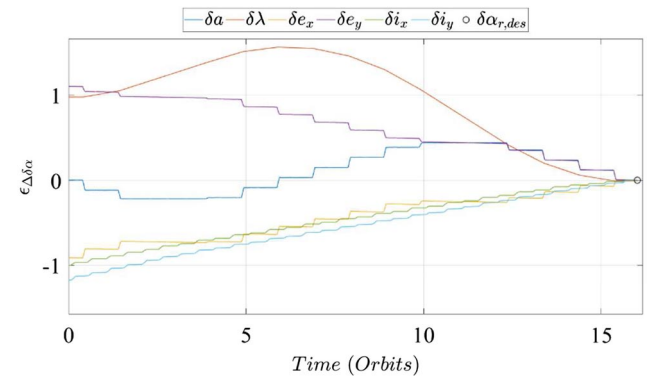
Fig. 14   Relative error $\epsilon_{\Delta \delta \alpha_r}(t)$ for test case 1.

2. Test Case 2

To avoid the deputy spacecraft entering the chief safety zone, the path constraints discussed in Sec. III.C are included in the MILP formulation. Figure 16 shows the corresponding control acceleration profile. As it is clear from the figure, the optimizer modifies only the along-track control, mainly adding one thruster firing with respect to test case 1 (i.e., finite-time maneuvers are 46). Moreover, it is worth noting that the along-track finite-time maneuvers are spread around $u_c = (1/\beta)(\mathrm{atan}(\Delta \delta e_y / \Delta \delta e_x) + k_j \pi - C u_T)$, where $k_j \in \mathbb{N}$, even though they are not centered at the aforementioned value of mean

Table 4   Accuracies for test case 1

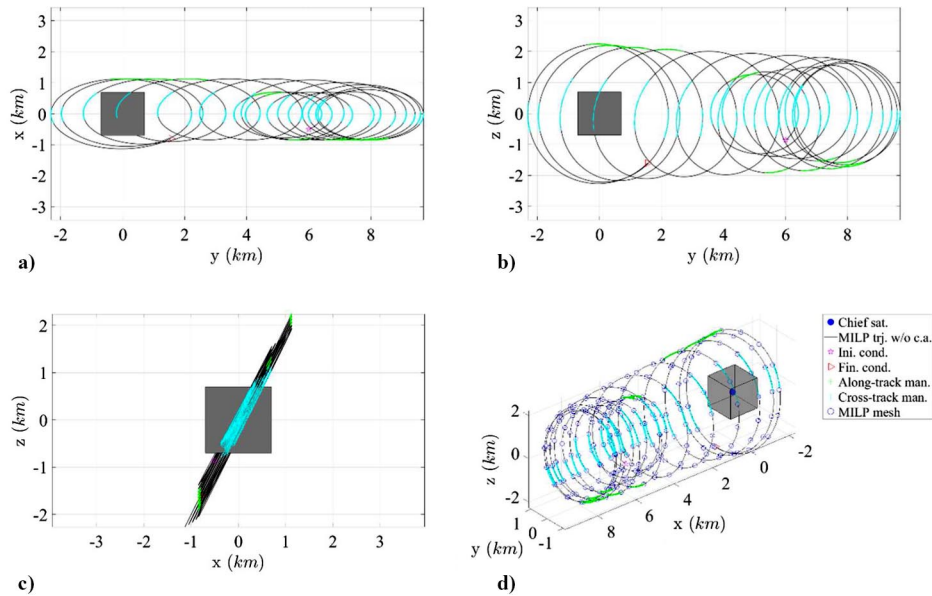| Accuracy metric	Value
$\lvert \epsilon_{\Delta \delta a}(T) \rvert a_{c,0}$, m	1.230×10^{-3}
$\lvert \epsilon_{\Delta \delta \lambda}(T) \rvert a_{c,0}$, m	8.375×10^{-3}
$\lvert \epsilon_{\Delta \delta e_x}(T) \rvert a_{c,0}$, m	1.282×10^{-3}
$\lvert \epsilon_{\Delta \delta e_y}(T) \rvert a_{c,0}$, m	1.054×10^{-3}
$\lvert \epsilon_{\Delta \delta i_x}(T) \rvert a_{c,0}$, m	1.00×10^{-3}
$\lvert \epsilon_{\Delta \delta i_y}(T) \rvert a_{c,0}$, m	0.591×10^{-3}

Fig. 15   Relative motion trajectory (Fig. 15d) for test case 1: a) x–y, b) z–y, and c) z–x views of the trajectory.
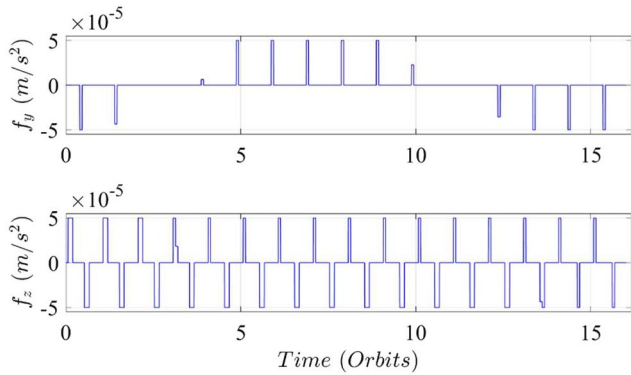

Fig. 16   Acceleration profile for test case 2.

argument of latitude. On the contrary, the cross-track maneuvers are performed around $u_c = (1/\beta)(\text{atan}(\Delta \delta i_y / \Delta \delta i_x) + k_j \pi - C u_T)$; see also Fig. 17a. The new proposed control strategy requires the same delta-v of case 1. Figure 17 illustrates the deputy trajectory in the

chief RTN reference frame (see Fig. 17d) along with its views on x–y (see Fig. 17a), z–y (see Fig. 17b), and z–x (see Fig. 17c) planes. All points of the time mesh (blue circles) lie outside the defined safety volume, proving the effectiveness of the proposed constraint formulation. It is worth remarking that the minimum-fuel MILP solution is computed using the linear dynamics model discussed in Sec. II.A, whereas the depicted trajectory is obtained using high-accuracy orbital propagator. This fact entails a slight displacement of the mesh points from the real trajectory.

According to Eq. (68), Fig. 18 illustrates the relative error along the reconfiguration maneuver interval. The derived control solution allows the achievement of the desired formation configuration in 16 chief orbital periods, with a total final relative error of 8.705×10^{-3} m [see Eq. (30)]. The details of relative error for each ROE vector element are reported in Table 5. Comparing the results reported in Fig. 18 with those illustrated in Fig. 14, it turns out that the in-plane components of the ROE vector are mainly affected by the introduction of the path constraints. In fact, because of the slight coupling between the in-plane and out-of-plane dynamics [see the plant matrix A_{NC} reported in Eq. (8)], changing the along-track control profile must have an impact mainly on δa, $\delta \lambda$, δe_x, and δe_y.
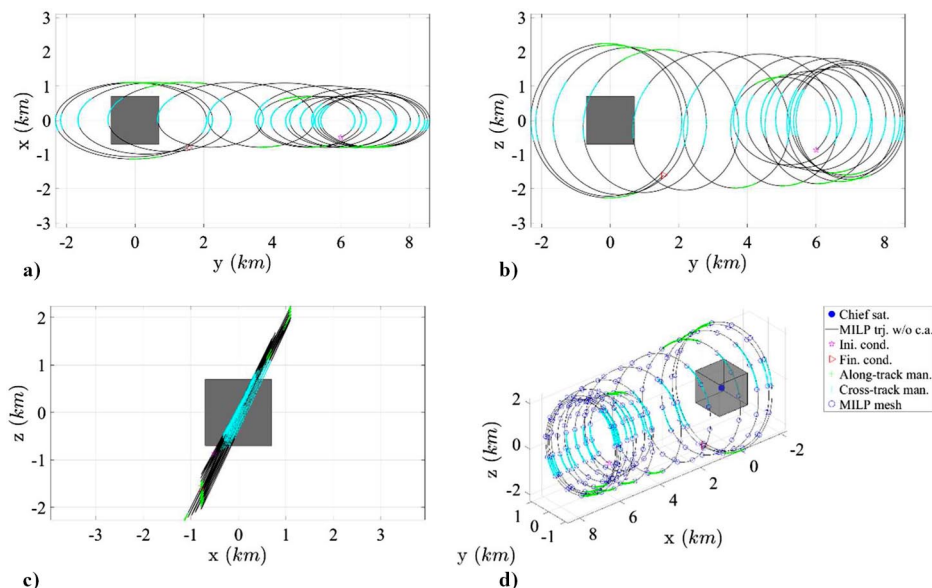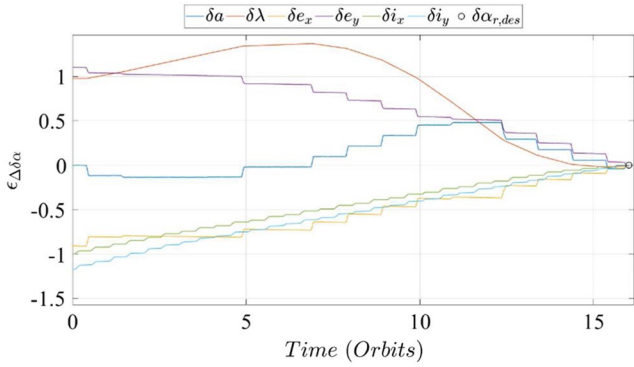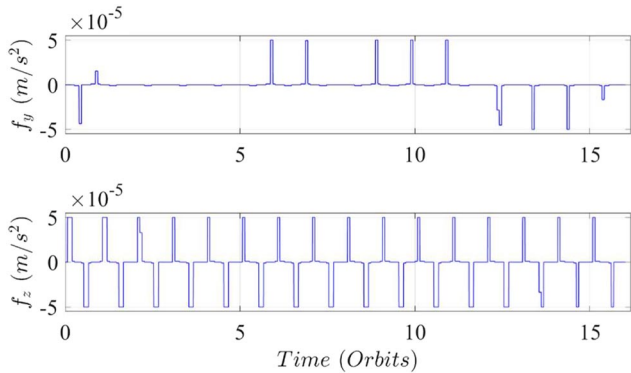

Fig. 17   Relative motion trajectory (Fig. 17d) for test case 2: a) x–y, b) z–y, and c) z–x views of the trajectory.

Table 5   Accuracies for test case 2

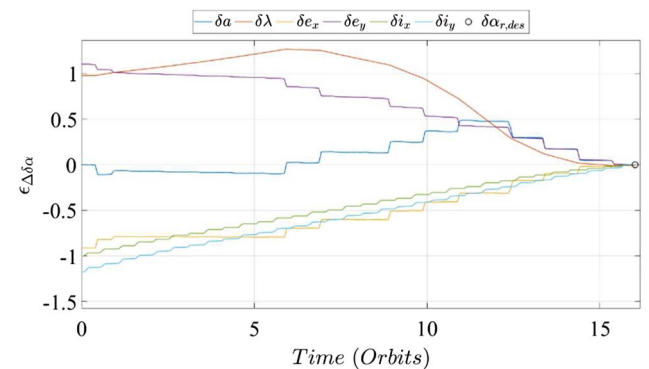| Accuracy metric	Value
$|\epsilon_{\Delta\delta a}(T)|a_{c,0}$, m	1.230×10^{-3}
$|\epsilon_{\Delta\delta\lambda}(T)|a_{c,0}$, m	8.312×10^{-3}
$|\epsilon_{\Delta\delta e_x}(T)|a_{c,0}$, m	1.088×10^{-3}
$|\epsilon_{\Delta\delta e_y}(T)|a_{c,0}$, m	0.729×10^{-3}
$|\epsilon_{\Delta\delta i_x}(T)|a_{c,0}$, m	1.04×10^{-3}
$|\epsilon_{\Delta\delta i_y}(T)|a_{c,0}$, m	0.514×10^{-3}

Finally, it is worth pointing out that CPLEX provides the solution in about 19.07 s. Then, the inclusion of path constraints penalizes the computing performance of MILP algorithm.
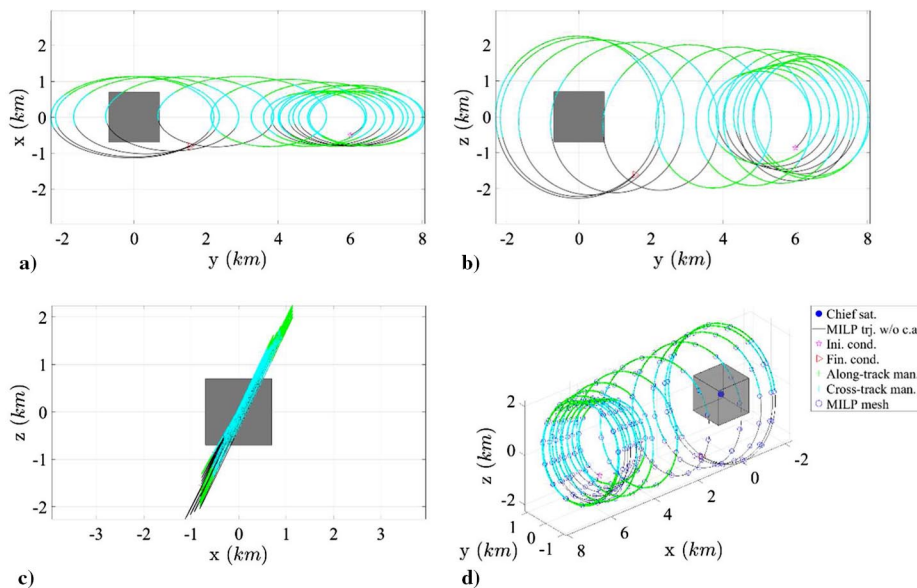
3. Test Case 3

This test case includes the constraints presented in Sec. III.C, along with the collision avoidance constraints defined in Sec. III.B. Here, it is imposed that the control profile consists of 10 thrusters' firings (i.e., $N_I = 10$) at most, and the propulsion system operates at least for about 1/3 of the chief orbital periods (i.e., $N_s = 5$, in accordance with the number of subintervals chosen and the maneuvering interval). Moreover, a minimum time separation between two consecutive firings of 30 min is enforced by setting $N_t = 5$.

Figure 19 shows the control profile obtained by the MILP solver. Accordingly, both in-plane and out-of-plane profiles are modified with respect to the test case 2, resulting in a 10 thrusters firing reconfiguration strategy. It is worth observing that the inclusion of the operational and time constraints slightly degrades the performance of the reconfiguration strategy, leading to a total delta-v of 1.225 m/s.

Figure 20 shows the relative trajectory (see Fig. 20d) along with its projections on the planes x–y (see Fig. 20a), y–z (see Fig. 20b), and x–z (see Fig. 20c). As for test case 2, also in this simulation the deputy trajectory lies outside the screening volume of the chief. In addition, the along-track finite-time maneuvers occur in

Fig. 18   Relative error $\epsilon_{\Delta\delta\alpha_r}(t)$ for test case 2.

Fig. 19   Acceleration profile for test case 3.

Fig. 21   Relative error $\epsilon_{\Delta\delta\alpha_r}(t)$ for test case 3.

Fig. 20   Relative motion trajectory (Fig. 20d) for test case 3: a) x–y, b) z–y, and c) z–x views of the trajectory.

Table 6　　Accuracies for test case 4

Accuracy metric	Value
$\|\epsilon_{\Delta\delta a}(T)\|a_{c,0}$, m	1.216×10^{-3}
$\|\epsilon_{\Delta\delta\lambda}(T)\|a_{c,0}$, m	8.408×10^{-3}
$\|\epsilon_{\Delta\delta e_x}(T)\|a_{c,0}$, m	1.145×10^{-3}
$\|\epsilon_{\Delta\delta e_y}(T)\|a_{c,0}$, m	0.732×10^{-3}
$\|\epsilon_{\Delta\delta i_x}(T)\|a_{c,0}$, m	1.082×10^{-3}
$\|\epsilon_{\Delta\delta i_y}(T)\|a_{c,0}$, m	0.469×10^{-3}

proximity of $u_c = (1/\beta)(\mathrm{atan}(\Delta\delta e_y/\Delta\delta e_x) + k_j\pi - Cu_T)$, whereas the cross-track maneuvers are performed around the mean argument of latitude $u_c = (1/\beta)(\mathrm{atan}(\Delta\delta i_y/\Delta\delta i_x) + k_j\pi - Cu_T)$, where $k_j \in \mathbb{N}$.

Finally, Fig. 21 depicts the relative error corresponding, $\epsilon_{\Delta\delta\alpha_r}(t)$ (with $r = 1, \ldots, 6$), over the maneuvering interval. As expected, all components of the ROE vector change with respect to test case 2 (see Fig. 18) because the both in-plane and out-of-plane acceleration profiles are modified. However, a final relative accuracy of order of millimeter is achieved, as shown in Table 6.

It is worth noting that the computing time increases considerably, reaching the value of 2.74 min. In fact, in this case the MILP formulation involves 1916 integer variables more than test case 2 and requires satisfying 1427 additional inequalities with respect to test case 2.

V.　Conclusions

This paper addressed the design of the minimum-fuel maneuvering strategy for the spacecraft formation reconfiguration in J_2-perturbed near-circular orbit. The reconfiguration problem has been formulated as an optimal control problem, assuming that the maneuverable spacecraft can perform only a series of constant finite-time maneuvers to control the relative configuration (i.e., the control acceleration profile is assumed to be a piecewise constant function over the maneuvering interval).

The aforementioned optimal control problem has been formulated as a mixed-integer linear programming (MILP) problem; the maneuvering interval has been discretized to cancel the nonlinearities related to the boundary conditions, and an additional set of optimization parameters have been introduced to make the objective function linear. Moreover, the collision avoidance and the maneuvering time constraints dictated by mission operations have been considered to make the MILP-based approach suited to handle the requirements coming from a realistic flight scenario. The simulation results have demonstrated the effectiveness of the MILP framework for the design of the minimum-fuel reconfiguration maneuver. When the MILP solution is added to the deputy nonlinear dynamics, the final formation configuration is achieved with the accuracy of order of millimeter.

Moreover, the analyses carried out have shown that the computational performances of MILP solver are affected by complexity of the problem, besides the number of optimization variables and inequalities constraints. In fact, when the collision avoidance and the additional time constraints are included in the formulation, the solver finds a feasible control solution in more than 2 min. On the contrary, if only the limitations on the control acceleration are taken into account, the MILP approach is able to provide the control scheme in less than 30 s, regardless of the chosen time mesh size.

Finally, the MILP-based approach presented in this paper is a systematic method to derive the minimum-fuel maneuvering scheme to reconfigure a two-satellite formation. Moreover, if neither constraints on the spacecraft path or operational time requirements need to be met, the proposed approach can be implemented onboard.

Appendix: Control Influence Matrix

The elements of the control influence matrix $\mathbf{\Gamma}_F$ [see Eq. (4)] are

$$\gamma_{13} = \gamma_{51} = \gamma_{52} = \gamma_{61} = \gamma_{62} = 0$$

$$\gamma_{11} = \frac{2e_d s_{f_d}}{n_d\eta_d a_c}, \quad \gamma_{12} = \frac{2(1 + e_d c_{f_d})}{n_d\eta_d a_c}$$

$$\gamma_{21} = -\frac{\eta_d e_d c_{f_d}}{a_d n_d(1 + \eta_d)} - \frac{2\eta_d^2}{a_d n_d(1 + e_d c_{f_d})}$$

$$\gamma_{22} = -\frac{\eta_d e_d[(2 + e_d c_{f_d})s_{f_d}]}{a_d n_d(1 + \eta_d)(1 + e_d c_{f_d})}, \quad \gamma_{23} = -\frac{\eta s_{\theta_d}(c_{i_c} - c_{i_d})}{a_d n_d(1 + e_d c_{f_d})s_{i_d}}$$

$$\gamma_{31} = \frac{\eta_d s_{\theta_d}}{a_d n_d}, \quad \gamma_{32} = \frac{\eta_d(2 + e_d c_{f_d})c_{\theta_d} + \eta_d e_{xd}}{a_d n_d(1 + e_d c_{f_d})}$$

$$\gamma_{33} = \frac{\eta_d e_{yd} s_{\theta_d} \cot g(i_d)}{a_d n_d(1 + e_d c_{f_d})}, \quad \gamma_{41} = -\frac{\eta_d c_{\theta_d}}{a_d n_d}$$

$$\gamma_{42} = \frac{\eta_d(2 + e_d c_{f_d})s_{\theta_d} + \eta_d e_{yd}}{a_d n_d(1 + e_d c_{f_d})}, \quad \gamma_{43} = -\frac{\eta_d e_{xd} s_{\theta_d} \cot g(i_d)}{a_d n_d(1 + e_d c_{f_d})}$$

$$\gamma_{53} = \frac{\eta_d s_{\theta_d}}{a_d n_d(1 + e_d c_{f_d})}, \quad \gamma_{63} = \frac{\eta_d c_{\theta_d} s_{i_c}}{a_d n_d(1 + e_d c_{f_d})s_{i_d}} \tag{A1}$$

where f_d and $\theta_d = f_d + \omega_d$ represent the deputy satellite's true anomaly and true argument of latitude, respectively. The symbols $s_{(\cdot)}$ and $c_{(\cdot)}$ denote the $\sin(\cdot)$ and $\cos(\cdot)$ functions, respectively.

References

[1] Di Mauro, G., Lawn, M., and Bevilacqua, R., "Survey on Guidance Navigation and Control Requirements for Spacecraft Formation-Flying Missions," *Journal of Guidance, Control, and Dynamics*, Vol. 41, No. 3, 2018.
doi:10.2514/1.G002868

[2] Gaias, G., and D'Amico, S., "Impulsive Maneuvers for Formation Reconfiguration Using Relative Orbital Elements," *Journal of Guidance, Control, and Dynamics*, Vol. 38, No. 6, 2015, pp. 1036–1049.
doi:10.2514/1.G000189

[3] Chernick, M., and D'Amico, S., "New Closed-Form Solutions for Optimal Impulsive Control of Spacecraft Relative Motion," *Journal of Guidance, Control, and Dynamics*, Vol. 41, No. 2, 2018, pp. 301–319.
doi:10.2514/1.G002848

[4] Vaddi, S., Alfriend, K., Vadali, S., and Sengupta, P., "Formation Establishment and Reconfiguration Using Impulsive Control," *Journal of Guidance Control, and Dynamics*, Vol. 28, No. 2, 2005, pp. 262–268.
doi:10.2514/1.6687

[5] Roscoe, C. W. T., Westphal, J. J., Griesbach, J. D., and Schaub, H., "Formation Establishment and Reconfiguration Using Differential Elements in J2-Perturbed Orbits," *Journal of Guidance, Control, and Dynamics*, Vol. 38, No. 9, 2015, pp. 1725–1740.
doi:10.2514/1.G000999

[6] Ben Larbi, M. K., and Bergner, P., "Concept for the Control of Relative Orbital Elements for Non-Impulsive Thrust Maneuver," *1st IFAC Workshop on Embedded Guidance, Navigation and Control in Aerospace*, Vol. 45, No. 1, 2012, pp. 41–46.
doi:10.3182/20120213-3-IN-4034.00010

[7] Di Mauro, G., Spiller, D., Bevilacqua, R., Sullivan, J., and D'Amico, S., "Continuous Maneuvers of Spacecraft Formation Flying Reconfiguration Using Relative Orbit Elements," *Acta Astronautica*, March 2018.
doi:10.1016/j.actaastro.2018.01.043

[8] Acikmese, B., Scharf, D., Hadaegh, F., and Murray, E., "A Convex Guidance Algorithm for Formation Reconfiguration," *AIAA Guidance, Navigation, and Control Conference and Exhibit*, AIAA Paper 2006-6070, Aug. 2006.
doi:10.2514/6.2006-6070

[9] Huntington, G. T., and Rao, A. V., "Optimal Reconfiguration of Spacecraft Formations Using the Gauss Pseudospectral Method," *Journal of Guidance, Control, and Dynamics*, Vol. 31, No. 3, 2008, pp. 689–698.
doi:10.2514/1.31083

[10] Wu, B.-L., Wang, D.-W., and Poh, E.-K., "Energy-Optimal Low-Thrust Satellite Formation Manoeuvre in Presence of J2 Perturbation," *Journal of Aerospace Engineering*, Vol. 225, No. 9, 2011, pp. 961–968.
doi:10.1177/0954410011408659

[11] Richards, A., Schouwenaars, T., How, J. P., and Feron, E., "Spacecraft Trajectory Planning with Avoidance Constraints Using Mixed-Integer Linear Programming," *Journal of Guidance, Control, and Dynamics*, Vol. 25, No. 4, 2002, pp. 755–764.
doi:10.2514/2.4943

[12] D'Amico, S., "Autonomous Formation Flying in Low Earth Orbit," Ph.D. Dissertation, Univ. of Delft, Delft, The Netherlands, 2010.

[13] Zhong, W., and Gurfil, P., "Mean Orbital Elements Estimation for Autonomous Satellite Guidance and Orbit Control," *Journal of Guidance, Control, and Dynamics*, Vol. 36, No. 6, 2013, pp. 1624–1641.
doi:10.2514/1.60701

[14] Sullivan, J., Koening, A. W., and D'Amico, S., "Improved Maneuver Free Approach Angles-Only Navigation for Space Rendezvous," *Proceeding of the 26th AAS/AIAA Spaceflight Mechanics*, Vol. 158, Univelt, Inc., Escondido, CA, 2016, pp. 1161–1184.

[15] Di Mauro, G., Spiller, D., Bevilacqua, R., and Curti, F., "Optimal Continuous Maneuvers for Satellite Formation Reconfiguration in J2-Perturbed Orbits," *2018 Space Flight Mechanics Meeting*, AIAA Paper 2016-0216, 2016.
doi:10.2514/6.2018-0216

[16] Longuski, J. M., Guzman, J. J., and Prussing, J. E., *Optimal Control with Aerospace Applications*, Springer, New York, 2014, pp. 19–28.

[17] D'Amico, S., "Relative Orbital Elements as Integration Constants of Hill's Equations," Deutsches Zentrum für Luft- und Raumfahrt, Oberpfaffenhofen DLR-GSOC TN 05-08, Oberpfaffenhofen, Germany, 2005.

[18] Gaias, G., Ardaens, J.-S., and Montenbruck, O., "Model of J2 Perturbed Satellite Relative Motion with Time-Varying Differential Drag," *Celestial Mechanics and Dynamical Astronomy*, Vol. 123, No. 4, 2015, pp. 411–433.
doi:10.1007/s10569-015-9643-2

[19] Vallado, D., *Fundamentals of Astrodynamics and Applications*, Springer–Verlag, New York, 1997, pp. 1–94.

[20] Alfried, K., Vadali, S. R., Gurfil, P., How, J., and Breger, L., *Spacecraft Formation Flying: Dynamics, Control and Navigation*, Butterworth-Heinemann, Oxford, England, U.K., 2010, pp. 1–11.

[21] Schaub, H., and Junkins, J., *Analytical Mechanics of Space Systems*, AIAA, Reston, VA, 2009, pp. 696–777.
doi:10.2514/4.867231

[22] Nocedal, J., and Wright, S. J., *Numerical Optimization*, Springer, New York, 2006, pp. 30–132.

[23] Pasopoulos, K. E., and Vrahatis, M. N., *Particle Swarm Optimization and Intelligence: Advances and Applications*, Information Science Reference, Hershey, PA, 2010, pp. 25–130.

[24] Deepa, S. N., and Sivanandam, S. N., *Introduction to Genetic Algorithms*, Springer, New York, 2008, pp. 15–37.
doi:10.1007/978-3-540-73190-0_7

[25] Wolsey, L. A., *Integer Programming*, Wiley, Hoboken, NJ, 1998, pp. 1–33, 91–134.

[26] Luenberger, D. G., and Ye, Y., *Linear and Nonlinear Programming*, Springer, New York, 2008, pp.11–143.

[27] Floudas, C. A., *Nonlinear and Mixed-Integer Optimization: Fundamentals and Applications*, Oxford Univ. Press, New York, 1995, pp. 95–107.

[28] FICO, "FICO Xxpress Mosel User Guide Ver 4.8," Fair Isaac Corp., San Jose, CA, Oct. 2017, Chaps. 1–3, 4.

[29] Gurobi, "Gurobi Optimizer Reference Manual Ver 8.1," Gurobi Optimization, LLC, Beaverton, OR, 2017, Chap. 13.

[30] IBM, "IBM ILOG CPLEX Optimization Studio CPLEX User's Manual," IBM ILOG, Ver 12 (Release 6), New York, 2015, Chap. 7.

[31] Brouwer, D., "Solution of the Problem of Artificial Satellite Theory Without Drag," *Astronautical Journal*, Vol. 64, No. 1274, 1959, pp. 378–397.
doi:10.1086/107958

[32] Lyddane, R., "Small Eccentricities or Inclinations in the Brouwer Theory of the Artificial Satellite," *Astronomical Journal*, Vol. 68, No. 8, 1963, pp. 555–558.
doi:10.1086/109179

[33] Riggi, L., and D'Amico, S., "Optimal Impulsive Closed-Form Control for Spacecraft Formation Flying and Rendezvous," *Proceeding of 2016 American Control Conference*, IEEE Publ., Piscataway, NJ, 2016, pp. 5854–5861.
doi:10.1109/ACC.2016.7526587

[34] Spiller, D., Ansalone, L., and Curti, F., "Particle Swarm Optimization for Time-Optimal Spacecraft Reorientation with Keep-Out Cones," *Journal of Guidance, Control, and Dynamics*, Vol. 39, No. 2, 2016, pp. 312–325.
doi:10.2514/1.G001228

[35] Tummala, A. R., and Dutta, A., "An Overview of Cube-Satellite Propulsion Technologies and Trends," *Aerospace*, Vol. 4, No. 4, 2017, p. 58.
doi:10.3390/aerospace4040058

[36] Krejci, D., and Paulo, L., "Space Propulsion Technology for Small Spacecraft," *Proceedings of the IEEE*, Vol. 106, No. 4, IEEE Publ., Piscataway, NJ, 2018, pp. 362–378.
doi:10.1109/JPROC.2017.2778747